The Astrophysical Journal, 933:74 (17pp), 2022 July 1 https://doi.org/10.3847/1538-4357/ac713e

Microphysics of Relativistic Collisionless Electron-ion-positron Shocks

Daniel Grošelj[1], Lorenzo Sironi[1], and Andrei M. Beloborodov[2,3]
[1] Department of Astronomy and Columbia Astrophysics Laboratory, Columbia University, New York, NY 10027, USA; daniel.groselj@columbia.edu
[2] Physics Department and Columbia Astrophysics Laboratory, Columbia University, New York, NY 10027, USA
[3] Max Planck Institute for Astrophysics, D-85741 Garching, Germany
Received 2022 February 2; revised 2022 May 4; accepted 2022 May 17; published 2022 July 5

Abstract

We perform particle-in-cell simulations to elucidate the microphysics of relativistic weakly magnetized shocks loaded with electron-positron pairs. Various external magnetizations $\sigma \lesssim 10^{-4}$ and pair-loading factors $Z_{\pm} \lesssim 10$ are studied, where $Z_{\pm}$ is the number of loaded electrons and positrons per ion. We find the following: (1) The shock becomes mediated by the ion Larmor gyration in the mean field when σ exceeds a critical value $\sigma_{\rm L}$ that decreases with $Z_{\pm}$. At $\sigma \lesssim \sigma_{\rm L}$ the shock is mediated by particle scattering in the self-generated microturbulent fields, the strength and scale of which decrease with $Z_{\pm}$, leading to lower $\sigma_{\rm L}$. (2) The energy fraction carried by the post-shock pairs is robustly in the range between 20% and 50% of the upstream ion energy. The mean energy per post-shock electron scales as $\overline{E}_{\rm e} \propto (Z_{\pm}+1)^{-1}$. (3) Pair loading suppresses nonthermal ion acceleration at magnetizations as low as $\sigma \approx 5 \times 10^{-6}$. The ions then become essentially thermal with mean energy $\overline{E}_{\rm i}$, while electrons form a nonthermal tail, extending from $E \sim (Z_{\pm}+1)^{-1}\overline{E}_{\rm i}$ to $\overline{E}_{\rm i}$. When $\sigma = 0$, particle acceleration is enhanced by the formation of intense magnetic cavities that populate the precursor during the late stages of shock evolution. Here, the maximum energy of the nonthermal ions and electrons keeps growing over the duration of the simulation. Alongside the simulations, we develop theoretical estimates consistent with the numerical results. Our findings have important implications for models of early gamma-ray burst afterglows.

Unified Astronomy Thesaurus concepts: High energy astrophysics (739); Shocks (2086); Non-thermal radiation sources (1119); Plasma astrophysics (1261); Gamma-ray bursts (629)

1. Introduction

Relativistic collisionless shocks play a key role in gamma-ray bursts (GRBs), the most powerful explosions in the universe. The prompt GRB spectrum peaks around 1 MeV and is followed by softer afterglow emitted by the blast wave from the explosion, as it expands into the external medium. This external shock is weakly magnetized and ultrarelativistic, with a Lorentz factor exceeding 100, and gradually decelerates with time. Its key feature is the ability to heat the medium to a relativistic temperature and accelerate nonthermal particles to high energies, which results in broadband nonthermal afterglow radiation.

1.1. Pair Loading in External GRB Shocks

Over the past couple of decades, relativistic collisionless shocks have been studied in detail using first-principles kinetic simulations. This includes simulations of relativistic shocks propagating in a weakly magnetized electron-ion medium (see Section 1.2), which is expected around GRBs. However, existing simulations do not apply to the earliest and brightest phase of the GRB afterglow, emitted at radii $R \lesssim 10^{17}$ cm. At these radii, the prompt gamma-rays streaming ahead of the blast wave load the external medium with copious electron-positron pairs (Thompson & Madau 2000; Mészáros et al. 2001; Beloborodov 2002). The number of loaded electrons and positrons per ion, $Z_{\pm}$, is independent of the original plasma density and can be accurately calculated for any GRB with a known (observed) prompt gamma-ray spectrum (Beloborodov 2002; Beloborodov et al. 2014). This calculation gives $Z_{\pm} > 1$ at radii $R \lesssim R_{\pm} \approx 10^{17}(\mathcal{E}/10^{54}\ {\rm erg})^{1/2}$ cm, where $\mathcal{E}$ is the isotropic equivalent of the GRB energy. At radii $R \ll R_{\pm}$, the pair-loading factor $Z_{\pm}$ reaches extremely high values, exceeding 10^4, and drops to $Z_{\pm} < 1$ when the blast wave expands to $R \gtrsim R_{\pm}$. In addition to the pair loading by the prompt megaelectronvolt radiation, pairs can be created by gamma-rays emitted by the shock itself (Derishev & Piran 2016).

When $Z_{\pm} \ll m_{\rm i}/m_{\rm e} \approx 1836$ (the proton-electron mass ratio), the plasma rest mass is dominated by the ions rather than pairs. On the other hand, even a modest $Z_{\pm}$ of a few can qualitatively change the shock physics because it introduces light charges of both signs. This can affect the strength of magnetic fields generated in the shock and the mechanism of particle energization. Moreover, when the shock energy budget is dominated by the ions, it is important to know what fraction $\epsilon_{\rm e}$ of the initial ion energy will be given to the post-shock electrons and positrons (which can efficiently radiate) and what nonthermal tail should be expected in the downstream particle distribution.

Answers to these questions have strong implications for the expected early afterglow of GRBs. In particular, Beloborodov et al. (2014) proposed that the pair-loading factor $Z_{\pm}(R)$ shapes the evolution of early gigaelectronvolt emission detected in GRBs (Ackermann et al. 2013). Their calculations assumed that the emission is dominated by hot pairs with $\epsilon_{\rm e} \approx 0.3$ when $1 \lesssim Z_{\pm} \ll m_{\rm i}/m_{\rm e}$, neglecting any nonthermal tails. This simple model was found consistent with observations of seven GRBs with good early gigaelectronvolt data, and was further confirmed by the optical data available for two bursts (Hascoët et al. 2015).

In order to improve confidence in models of the early GRB afterglow emission, it is important to constrain from first principles the relevant shock microphysics, such as the downstream pair energy fraction. To this end, we perform a set of particle-in-cell (PIC) simulations of collisionless weakly magnetized relativistic shocks, treating $Z_\pm$ as a fixed parameter for the upstream plasma. Our simulations are local in the sense that the scales involved are much smaller than the shock radius R. We will show below that even moderate pair-loading factors of order unity significantly affect the structure of the shock on kinetic scales and the resulting particle acceleration, whereas the pair energy fraction ϵ_e is rather insensitive to the changes in particle composition.

1.2. Previous Simulations

Kinetic simulations of relativistic electron-ion and electron-positron weakly magnetized shocks (e.g., Sironi et al. 2013; Plotnikov et al. 2018) demonstrate the key role of the magnetization σ, the ratio of the upstream Poynting to kinetic energy flux. Above a critical magnetization σ_L ($\sim 10^{-4}$ for electron-ion and $\sim 10^{-3}$ for electron-positron shocks) the incoming flow is stopped by the Larmor gyration of the particles in the downstream compressed mean magnetic field, which mediates the shock transition. The downstream particle energy distributions are essentially thermal.

For magnetizations $\sigma \lesssim \sigma_L$ the shock is mediated by plasma microinstabilities, most notably by the Weibel (filamentation) instability (Fried 1959; Weibel 1959; Medvedev & Loeb 1999; Silva et al. 2003; Achterberg & Wiersma 2007; Bret et al. 2014; Takamoto et al. 2018; Lemoine et al. 2019a). The Weibel instability is fueled by the anisotropy of the upstream particle momentum distribution, composed of the incoming background plasma and the counterstreaming beam of particles returning from the shock. It acts to exponentially amplify seed magnetic fields by channeling particles into elongated current filaments of alternating polarity, which provides positive feedback on the field perturbation. The filaments are elongated along the streaming direction and their typical thickness is comparable to the plasma skin depth.

During the nonlinear stage of the Weibel instability, incoming particles scatter off the self-generated turbulence, thereby isotropizing their momenta. This provides the mechanism that mediates the shock. A fraction of particles is reflected back and forth across the shock front, gaining energy upon each reflection in a first-order Fermi process (Blandford & Eichler 1987; Achterberg et al. 2001). Thus, Weibel-mediated relativistic shocks are efficient particle accelerators (Spitkovsky 2008a, 2008b; Martins et al. 2009; Nishikawa et al. 2009; Haugbølle 2011), In the electron-ion case, it has been also demonstrated that the incoming electrons are preheated to nearly 40% of the initial ion energy before entering the downstream (Spitkovsky 2008b; Sironi et al. 2013). Essentially, the preheating eliminates the disparity between the electron and ion plasma microscales, so that an electron-ion Weibel-mediated shock behaves qualitatively almost as if it were composed of electrons and positrons.

1.3. Scope of the Present Paper

While shocks in electron-positron and electron-ion plasmas have been studied in detail, only a limited number of simulations of electron-ion-positron shocks have been performed (Hoshino & Arons 1991; Hoshino et al. 1992; Amato & Arons 2006; Stockem et al. 2012), and all of them focused on moderate to high magnetizations, with applications to the termination shock of pulsar winds. This case is qualitatively different from the GRB blast waves that propagate in a very low-σ external medium.

Here, we perform kinetic simulations of *weakly magnetized*, relativistic pair-loaded shocks with the goal of understanding how the shock microphysics depends on the plasma composition. The simulations provide a fairly comprehensive view of the relevant parameter space, with magnetizations in the range $0 \leqslant \sigma \leqslant 10^{-4}$ and pair-loading factors $0 \leqslant Z_\pm \leqslant 12$. Our numerical effort is complemented by analytical estimates that help interpret the results.

This paper is organized as follows: In Section 2 we provide the numerical details of our shock simulations. We first demonstrate the role of pair loading in an idealized Weibel unstable plasma in Section 3. This simplified model helps to interpret the main results of our shock simulations, which are presented in Sections 4 and 5. Section 4 shows how the shock structure changes with respect to the pair-loading factor. In Section 5 we analyze the collisionless partitioning of energy between ions and pairs, and characterize their downstream energy spectra. The implications of our results for the early afterglow phase of GRBs are briefly discussed in Section 6. We conclude the paper with a summary of our main results in Section 7.

2. Simulation Setup

We carried out a series of two-dimensional (2D) PIC simulations of relativistic electron-ion-positron shocks using the code OSIRIS 4.0 (Fonseca et al. 2002, 2013). The simulations are performed for various pair-loading factors

$$Z_\pm \equiv \frac{2n_{0e^+}}{n_{0i}} \tag{1}$$

and magnetizations

$$\sigma \equiv \frac{B_0^2}{4\pi\gamma_0 n_{0i} m_i c^2}, \tag{2}$$

where n_{0i} is the ion density, n_{0e^+} the positron density, $\gamma_0 \gg 1$ is the Lorentz factor of the cold upstream flow, and B_0 is the mean shock-perpendicular magnetic field. Subscript "0" refers to the upstream plasma far ahead of the shock. All quantities are measured in the simulation frame, in which the shocked downstream plasma is at rest. We consider magnetizations in the range $0 \leqslant \sigma \leqslant 10^{-4}$ and pair-loading factors $0 \leqslant Z_\pm \leqslant 12$.

To save computational resources we opt for a reduced ion-electron mass ratio of $m_i/m_e = 36$. We mostly focus on pair-loading factors of order unity, such that the ions dominate the upstream momentum even at the reduced value of the mass ratio. Results from a simulation with $Z_\pm = 2$ and $m_i/m_e = 100$ are included for reference in Appendix A, showing good agreement with our fiducial case $m_i/m_e = 36$. The upstream magnetic field $\boldsymbol{B}_0 = B_0\,\hat{\boldsymbol{z}}$ points out of the 2D simulation plane.[4] We also initialize a motional electric field $\boldsymbol{E}_0 = -\boldsymbol{\beta}_0 \times \boldsymbol{B}_0$, where $\boldsymbol{\beta}_0 = -(1 - 1/\gamma_0^2)^{1/2}\,\hat{\boldsymbol{x}}$ is the initial

[4] In the weakly magnetized relativistic regime, the out-of-plane field orientation is preferred over the in-plane configuration because it best captures the physics of particle acceleration (Sironi et al. 2013).

three velocity of the upstream flow in units of c. The shock formation is triggered by the reflection of particles from a conducting wall located on the left side ($x = 0$) of the computational domain (e.g., see Spitkovsky 2008b; Martins et al. 2009; Sironi et al. 2013). The longitudinal size is chosen long enough to accommodate the propagating shock front until the end of the simulation. Periodic boundaries are used in the transverse y-direction. The transverse size of the domain is $31.4\,d_{\rm i}$, where $d_{\rm i} = c/\omega_{\rm pi} = (\gamma_0 m_{\rm i} c^2/4\pi n_{0{\rm i}} e^2)^{1/2}$ is the (upstream) relativistic ion skin depth.

The numerical details of our simulations are as follows: We set the resolution to eight cells per pair plasma skin depth $d_{\rm e} = c/\omega_{\rm pe} = (\gamma_0 m_{\rm e} c^2/4\pi n_{0{\rm e}} e^2)^{1/2}$, where $n_{0{\rm e}} = (Z_\pm + 1) n_{0{\rm i}}$ is the combined (upstream) density of electrons and positrons. Our time step is $\Delta t \omega_{\rm pe} = 1/16$. The calculations require significant resources because the scale separation, $\omega_{\rm pe}/\omega_{\rm pi} = [(Z_\pm + 1) m_{\rm i}/m_{\rm e}]^{1/2}$, grows with the amount of pair loading. For instance, our largest simulation spans about $295{,}000 \times 5400$ grid cells and is evolved over 600,000 time steps. Cubic spline macroparticle shapes and smoothing of the electric currents are used to reduce PIC noise and numerical heating. The electric current deposit is charge conserving. An electromagnetic field solver introduced by Blinne et al. (2018) is used to mitigate the numerical Cherenkov instability (Godfrey 1974; Godfrey & Vay 2013). Further details on the mitigation of Cherenkov instability are provided in Appendix B. The upstream plasma ahead of the shock is introduced by a moving particle injector that is initially located next to the reflecting wall, but moves away from it at the speed of light as time progresses. The injected particles are sampled from a distribution with bulk Lorentz factor $\gamma_0 = 50$ and with a thermal spread of $T_{0{\rm e}^-} = T_{0{\rm e}^+} = T_{0{\rm i}} = 4.8 \times 10^{-5} m_{\rm i} c^2$. The injected particle number is typically set to eight or 12 per cell per species. Higher spatial resolutions and larger numbers of particles per cell were tested, indicating a qualitative and quantitative convergence of our results.

3. Homogeneous Beam-symmetric System

To understand how the pair enrichment affects the structure of a weakly magnetized shock, it is instructive to consider first an idealized periodic system, broadly resembling the early stage of shock formation. We shall assume that the initial configuration consists of two symmetric, unmagnetized cold plasma shells streaming through each other. Each of the two shells is charge and current neutral and moves with a bulk Lorentz factor $\gamma_0 \gg 1$. The ions have a total simulation-frame density $n_{0{\rm i}}$ and the total density of electrons and positrons is $n_{0{\rm e}} = (Z_\pm + 1) n_{0{\rm i}}$. To focus on regimes where ions dominate the energy budget we impose $Z_\pm \ll m_{\rm i}/m_{\rm e}$.

The idealized configuration described above is prone to plasma streaming instabilities, the most prominent of which is in this context the Weibel (filamentation) instability (Weibel 1959; Fried 1959; Silva et al. 2003; Achterberg & Wiersma 2007; Kumar et al. 2015; Takamoto et al. 2018). Let us consider the effect of the pair-loading parameter $Z_\pm$ on the generation of Weibel fields. The pair-driven instability will grow first and saturate on pair plasma scales, followed by the slower ion response. At this point, the electrons and positrons can be reasonably approximated as an isotropic, relativistically hot background, whereas the counterstreaming ion beams are still cold. The ion Weibel instability grows initially over the hot electron (and positron) background at a maximum rate that depends only on the ion properties. For cold ion beams, the peak growth rate is $\Gamma \simeq \omega_{\rm pi}$, where $\omega_{\rm pi}$ is the relativistic ion plasma frequency (e.g., see Achterberg et al. 2007; Lemoine & Pelletier 2011). We will show below that, unlike the linear growth rate, the nonlinear saturation strength of ion Weibel fields depends strongly on $Z_\pm$ as a result of the screening of ion currents by the pair plasma background.

Saturation of the ion-driven instability proceeds as follows: the exponential Weibel field growth at a given beam-perpendicular wavenumber k stalls when the magnetic bounce frequency becomes comparable to the characteristic growth rate

$$\left(\frac{e\,\beta_{x0}\delta B_k k}{\gamma_0 m_i}\right)^{1/2} \simeq \Gamma_k, \tag{3}$$

where δB_k is the magnetic fluctuation amplitude of modes with wavenumber $\sim k$ and Γ_k is the growth rate. Condition (3) is known as the trapping criterion (Davidson et al. 1972). In principle, the field may be amplified further after the end of the linear, exponentially growing stage. A more generic but equivalent estimate of δB_k can be obtained by assuming that the maximum field strength is reached when all the available current has been used (Kato 2005; Gedalin et al. 2012). From Ampere's law it follows that

$$\delta B_k \simeq 2\pi e n_{0{\rm i}}/k. \tag{4}$$

The latter leads to the same qualitative conclusion. Namely, as the field energy grows, short-wavelength modes saturate first, followed by ever-increasing scales, up to the largest scale that can sustain growth.

The maximum scale over which the ion instability can grow at a rate close to the maximum ($\sim\omega_{\rm pi}$), hereafter denoted with $\lambda \simeq \pi/k_*$, is controlled by the electron (and positron) background (Achterberg et al. 2007; Kumar et al. 2015). For a relativistically hot and isotropic electron background, k_* is estimated as

$$k_* d_{\rm i} \simeq \left(\frac{\omega_{\rm pi}^2}{\tilde{\omega}_{\rm pe}^2}\right)^{-1/3}, \tag{5}$$

where $\tilde{\omega}_{\rm pe} = (4\pi e^2 n_{0{\rm e}}/\overline{\gamma}_{\rm e} m_{\rm e})^{1/2}$ and $\overline{\gamma}_{\rm e}$ is the mean electron (and positron) Lorentz factor. For a detailed derivation of expression (5) see Lyubarsky & Eichler (2006) and Achterberg & Wiersma (2007). We mention that the inhibition of field growth at wavenumbers $k \lesssim k_*$ originates from the screening of ion current filaments by the electrons (and positrons); a robust feature known to persist well beyond the linear stage of the instability (Achterberg et al. 2007; Ruyer et al. 2015b).

A rough estimate for the total magnetic energy at saturation can be obtained by noticing that the fluctuation amplitude is proportional to the scale over which the field grows. Thus, the dominant contribution comes from the largest scale. By evaluating (4) at $k = k_*$ we are led to

$$\epsilon_B \simeq \frac{1}{8}\left(\frac{\omega_{\rm pi}^2}{\tilde{\omega}_{\rm pe}^2}\right)^{2/3}, \tag{6}$$

where $\epsilon_B \equiv \delta B^2/8\pi n_{0i}\gamma_0 m_i c^2$ is the magnetic energy fraction. Equation (3) yields the same estimate of ϵ_B for $k = k_*$ with $\Gamma_{k_*} = \omega_{pi}/\sqrt{2}$ (Achterberg et al. 2007).[5]

In order to obtain a more concrete prediction for ϵ_B and λ we note that, as the ion instability proceeds, electrons are heated beyond their initial energy of $\gamma_0 m_e c^2$ by extracting a fraction $\epsilon_e \sim 0.1$ from the ions (Gedalin et al. 2012; Plotnikov et al. 2013; Kumar et al. 2015). Therefore, we anticipate that reasonable estimates can be obtained provided that $\overline{\gamma}_e$, which appears in the definition of $\tilde{\omega}_{pe}$, takes into account the ion-to-electron energy transfer. This brings the ratio $\omega_{pi}/\tilde{\omega}_{pe}$ closer to unity. By defining the pair energy fraction $\epsilon_e \equiv n_{0e}\overline{\gamma}_e m_e/n_{0i}\gamma_0 m_i$, we express the mean electron Lorentz factor as

$$\overline{\gamma}_e \simeq (Z_\pm + 1)^{-1}\gamma_0 \epsilon_e m_i/m_e. \quad (7)$$

The explicit inverse dependence on $Z_\pm + 1$ reflects the fact that the energy drawn from the ions is distributed among a larger number of the light charge carries with growing $Z_\pm$. Using relation (7) we can express the ratio of the squared plasma frequencies as

$$\frac{\omega_{pi}^2}{\tilde{\omega}_{pe}^2} = \frac{\overline{\gamma}_e m_e}{\gamma_0 m_i}(Z_\pm + 1)^{-1} = \epsilon_e (Z_\pm + 1)^{-2}. \quad (8)$$

This leads to the following estimates for the magnetic energy fraction and transverse coherence scale at saturation:

$$\epsilon_B \simeq \frac{1}{8}\epsilon_e^{2/3}(Z_\pm + 1)^{-4/3},\ \lambda/d_i \simeq \pi\epsilon_e^{1/3}(Z_\pm + 1)^{-2/3}. \quad (9)$$

The estimates predict saturation of the ion Weibel instability at lower field amplitudes and at smaller scales when the plasma is loaded with pairs.

To test the above predictions, we perform 2D PIC simulations using a periodic box of size $(L_x/d_i, L_y/d_i) = (125.6, 31.4)$ and a reduced ion-electron mass ratio of 100. The initial condition consists of two pair-loaded cold plasma beams. The beams have opposite momenta and equal, spatially uniform particle densities. We evolve the system using 32 particles per cell per species and a standard electromagnetic field solver. Other numerical parameters match those described in Section 2 for our shock simulations.

In all runs we observe the formation of filamentary structures in the magnetic field, as expected for the Weibel instability. An example is shown in Figure 1. A careful look at that same figure reveals also some mildly periodic patterns along the longitudinal direction, which could be a sign of current filament disruption via the drift-kink instability (Ruyer & Fiuza 2018; Vanthieghem et al. 2018).

The time evolution of the system is depicted in Figure 2. The fields generated by the electron (and positron) driven instabilities saturate in a few tens of pair plasma times and decay rapidly, followed by the creation of the longer-lasting ion Weibel fields. We remark that the linear stage of the ion Weibel instability is not seen clearly in our setup because it is preceded by the faster-growing pair-driven instabilities.[6]

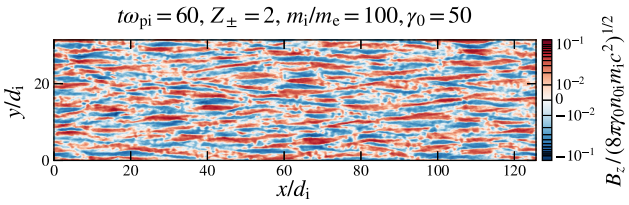

Figure 1. Structure of Weibel generated magnetic fields in a moderately pair-loaded plasma.

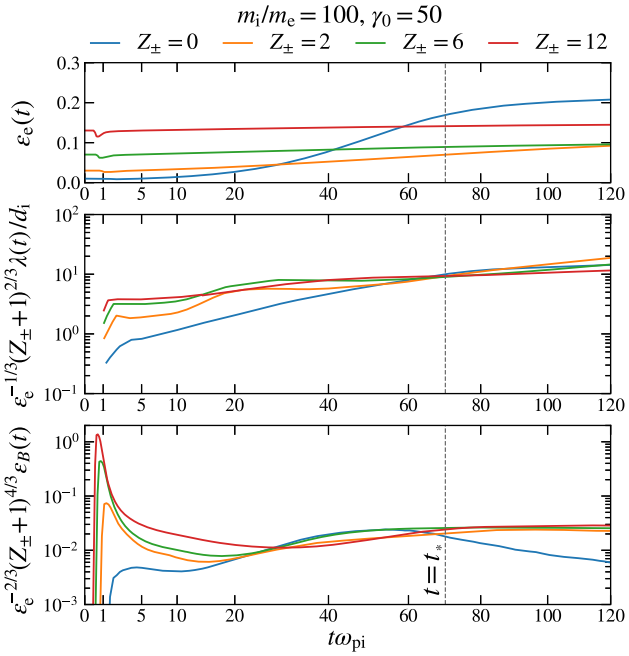

Figure 2. Time evolution of the Weibel instability in a pair-loaded plasma (see main text for details). The values of the mean magnetic energy fraction $\epsilon_B(t)$ and field coherence scale $\lambda(t)$ are compensated by the scaling predictions (9).

By the time $t_*\omega_{pi} \approx 70$ all simulations reach near maximum field strength of the ion Weibel instability (vertical dashed lines in Figure 2). We take this as the approximate time of saturation, at which we determine the pair energy fraction ϵ_e that is used to compensate the curves in the bottom two panels of Figure 2. The values of ϵ_e are at near maximum around $t \approx t_*$ and increase only slightly beyond this time. For $Z_\pm \geqslant 6$, the pair energy at saturation hardly exceeds the initial amount at the start of the simulation, given by $\epsilon_{e0} = (Z_\pm + 1)m_e/m_i$. More specifically, we find that the energy taken away from the ions and transferred to pairs, $\Delta\epsilon_e \approx \epsilon_e - \epsilon_{e0}$, is roughly inversely proportional to $Z_\pm + 1$ (not shown). As demonstrated below in Section 5.1, the heating of electrons and positrons in weakly magnetized pair-loaded shocks turns out to be more efficient than what is found in this idealized setup. When ϵ_e stops evolving, the screening wavenumber k_* (Equation (5)) becomes a constant. This sets the transverse magnetic field

[5] Both Equations (3) and (4) somewhat overpredict ϵ_B for the following reasons: Estimate (4) is based for simplicity on the total available current, whereas the actual current is some fraction of the total. In the case of Equation (3), we assume perfectly cold ion beams to estimate the growth rate, while in practice the growth rate may be reduced by the finite beam dispersion at the time when the largest scale of the instability is attained. Rather than the precise value of ϵ_B our main interest here is its dependence on $Z_\pm$. For this purpose, we find estimate (6) sufficient.

[6] To see the linear evolution of the ion instability, we performed additional simulations with initially isotropic and relativistically hot pairs and found growth rates $\Gamma \simeq \omega_{pi}$, as expected for the ion Weibel instability. Using this same setup, we also find that the linear stage of the ion instability ends at around 10 ion plasma times.

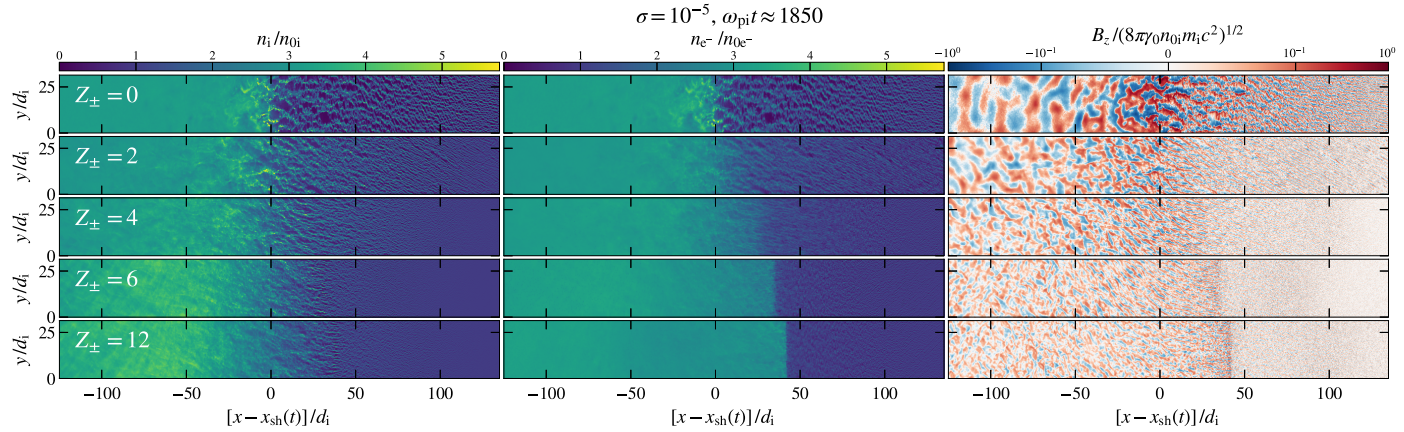

Figure 3. Shock structure as a function of pair-loading factor $Z_\pm$ at $\sigma = 10^{-5}$. Shown from left to right are the ion density, the electron density, and the out-of-plane magnetic field. We determine the shock position $x_{sh}(t)$ as the point where the y-averaged ion density exceeds the upstream value by a factor of 2.3.

coherence scale $\lambda \simeq \pi/k_*$ at the time of saturation of the ion instability.[7]

The main result of Figure 2 is that $\epsilon_B(t)$ and $\lambda(t)$ around the time $t \approx t_*$, when the ion Weibel fields reach maximum strength, are both nearly independent of $Z_\pm$ when compensated by the scaling predictions (9). Therefore, the PIC simulations confirm that the ion Weibel fields saturate at lower amplitudes and at smaller scales when the plasma is enriched with pairs. This result has important implications for the structure of weakly magnetized relativistic shocks with electron-ion-positron compositions, as shown in the following.

4. Shock Structure

We now turn to the shock structure as a function of the pair-loading factor. The key features are summarized in Figure 3, which shows a series of simulations at fixed magnetization $\sigma = 10^{-5}$ and for various pair-loading factors $Z_\pm$. The fields are visualized around $t\omega_{pi} \approx 1850$. It is evident that even moderate changes in the plasma composition significantly affect the shock structure. In qualitative agreement with the results of Section 3, the strength and scale of the self-generated magnetic turbulence drops with $Z_\pm$. Moreover, the filamentary structure of the precursor that is characteristic of a Weibel-mediated shock fades away as pairs are introduced into the upstream plasma.

4.1. Shock Width

The width of the ion shock, based on the y-averaged ion density profile, is seen to broaden from about $10\,d_i$ for $Z_\pm = 0$ to roughly $100\,d_i$ for $Z_\pm \geqslant 6$ (Figure 4, top panel). The reason for the broadening is that the microturbulence becomes inefficient in stopping the ion flow via particle scattering (see also Section 4.2). At sufficiently large pair-loading factors ($Z_\pm \geqslant 6$), the width of the ion shock approaches the ion Larmor radius in the downstream compressed mean magnetic field, $R_{L0}/d_i \simeq 1/3\sigma^{1/2} \approx 100$. Together with the shock structure shown in Figure 3, this suggests that the change in the plasma composition gives rise to a transition from a Weibel to a Larmor mediated shock at a fixed strength of the external magnetization.

[7] Here and in the rest of the paper, we employ a common definition of the coherence scale (e.g., Plotnikov et al. 2011) and calculate λ as the power-spectrum-weighted mean of π/k_y, where k_y is the transverse wavenumber.

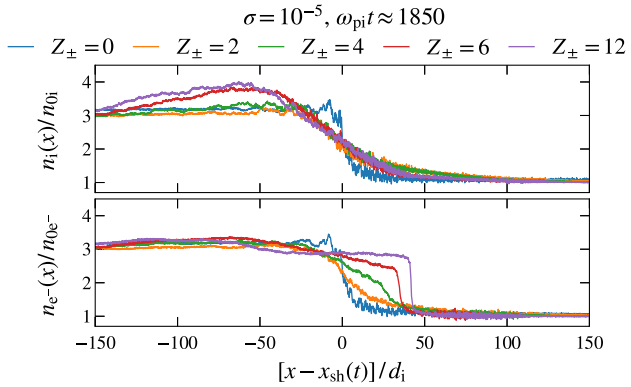

Figure 4. Shock density profiles for different pair-loading factors $Z_\pm$ at a fixed value of the magnetization $\sigma = 10^{-5}$.

The electrons and positrons (not shown) are seen to decouple from the ions with growing $Z_\pm$ and form a narrower subshock, as thin as a few d_i in width (at $Z_\pm = 12$), ahead of the broad ion density ramp (Figure 4, bottom panel). This is made possible by the fact that pairs carry lower inertia than the ions and are thus able to isotropize more rapidly than the ions when crossing the shock. In electron-ion shocks, electrostatic coupling prevents the formation of a narrower electron shock, even if the two species carry different relativistic inertia. In contrast, when the plasma is enriched with pairs, a fraction of the total electron charge is readily compensated by the positrons. This enables the light particles to decouple from the ions.

4.2. Particle Motion Across the Shock

To further elaborate on the mechanisms that mediate the shock transition at different values of the pair-loading parameter, we compare in Figure 5 the trajectories of particles crossing the shock for $Z_\pm = 0$ and $Z_\pm = 12$. The particle trajectories of the electron-ion shock ($Z_\pm = 0$) are considerably more chaotic and disperse rapidly with respect to the initial direction of motion. The electrons acquire a significant dispersion even before entering the shock, indicating heating in the upstream Weibel turbulence (Spitkovsky 2008b). Consistent with the phenomenology of Weibel-mediated shocks, a fraction of particles performs Fermi cycles, scattering back and forth across the shock (see also Spitkovsky 2008a; Martins et al. 2009).

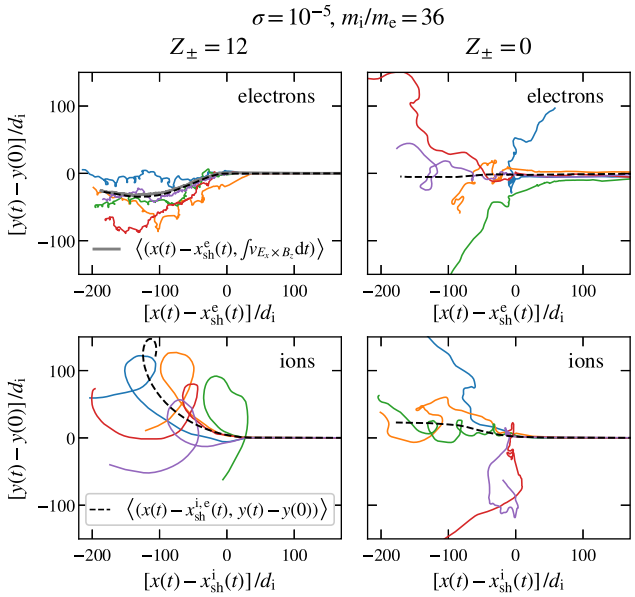

Figure 5. Sample trajectories of particles crossing a $\sigma = 10^{-5}$ shock for $Z_\pm = 12$ (left) vs. $Z_\pm = 0$ (right). Dashed curves in all panels show the ensemble-averaged trajectories. The position $x^{i,e}_{sh}(t)$ denotes the point where the y-averaged density of the species shown in a given panel exceeds the upstream value by a factor of 2.3. The gray curve in the top left panel shows the mean transverse displacement due to the $E_x \times B_z$ drift.

The motion of ions and electrons across the pair-loaded shock is significantly more ordered. The ions in particular display a very clear signature of Larmor gyration in the compressed mean field, which mediates the shock transition. The electrons show as well signs of gyration, but the typical scale of their motions is notably smaller than that of the ions, owing to the difference in inertia between the species. The disparity in inertia has another consequence. It gives rise to a charge separation across the ion shock transition, which generates a shock-parallel electric field (Lemoine & Pelletier 2011; Lemoine et al. 2019b). This E_x field is imprinted onto the electron trajectories shown in the top left panel of Figure 5 in the form of a transverse $E_x \times B_z$ drift (gray curve).

4.3. Energy Fraction and Scale of the Magnetic Fluctuations

It is worth asking how the results of our shock simulations can be reconciled with the theoretical estimates from Section 3, concerning the saturation of ion Weibel fields in a beam-symmetric system. In the upstream frame of the background plasma, the maximum ion Weibel instability growth rate is $\Gamma_u \simeq \omega_{pb}$ (e.g., see Lemoine & Pelletier 2010), where ω_{pb} is the beam-plasma frequency of the returning ions.[8] The latter is related to the background ion plasma frequency through the normalized (downstream frame) kinetic pressure of the beam ions

$$\xi_b \equiv \frac{P_b}{\gamma_0 n_{0i} m_i c^2} = \frac{\overline{\gamma}_b n_b (\Gamma_{ad} - 1)}{\gamma_0 n_{0i}}, \tag{10}$$

where $\overline{\gamma}_b$ is the mean Lorentz factor of the beam ions, n_b their density, and Γ_{ad} is the adiabatic index.[9] Assuming $\overline{\gamma}_b \simeq \gamma_0$, the beam-plasma frequency can be expressed as $\omega_{pb} = (4\pi e^2 n_b/\overline{\gamma}_b m_i)^{1/2} \simeq \xi_b^{1/2}\omega_{pi}$ (Pelletier et al. 2017). In effect, ξ_b quantifies the asymmetry of the beam-plasma system that is inherent to any realistic shock scenario.

As the incoming plasma moves toward the shock, it experiences a growing beam energy density and pressure, leading to a gradual slowdown of the background particles over the turbulent precursor. Instead of trying to describe the evolution over the entire precursor, we focus here on the generation of Weibel fields in the *near* upstream, because this is what largely controls the nature of magnetic fluctuations at the shock and further downstream. The region immediately ahead of the shock is also where the Weibel instability plays the most prominent role, given that it is the most robustly growing instability once the background electrons become hot (Lemoine & Pelletier 2011; Shaisultanov et al. 2012; Plotnikov et al. 2013).

In analogy with expression (5), the growth rate of the ion beam driven instability over a background with hot electrons and cold ions drops below the maximum for transverse wavenumbers $k \lesssim k_* \simeq \omega_{pb}^{1/3}\tilde{\omega}_{pe}^{2/3}/c$ (Lemoine & Pelletier 2011; Shaisultanov et al. 2012). Using the beam parameter ξ_b, the latter can be written as

$$k_* d_i \simeq \xi_b^{1/6}\left(\frac{\omega_{pi}^2}{\tilde{\omega}_{pe}^2}\right)^{-1/3}. \tag{11}$$

The expression applies to transverse wavenumbers and as such it is frame independent. It is obtained without taking into account the relative drift between the background species, which is appropriate for $Z_\pm = 0$ since the background electrons and ions are in this case tightly coupled. With a growing amount of pair loading, the motion of the background pairs becomes progressively more decoupled from the ions, as discussed in Sections 4.1 and 4.2. On this note, we mention that if the instability were to be driven exclusively by the streaming between the cold background ions (instead of beam ions) and the hot background pairs, the screening wavenumber would be given by Equation (5), which is only marginally different from Equation (11). A more detailed investigation of this aspect is left for future works. It is also worth commenting on the possibility that the field coherence scale is ultimately determined by the rate of current filament mergers over the length scale of the precursor (Medvedev et al. 2005; Stockem Novo et al. 2015; Ruyer et al. 2017), rather than by the local screening effect. In this regard, we mention that filament merger is a slow process on scales exceeding the screening wavelength (Achterberg et al. 2007), whereas the limited precursor length in a relativistic shock requires a rather fast-growing mechanism. Thus, in the relativistic case it seems reasonable to approximate the near-upstream coherence scale with $\lambda \simeq \pi/k_*$ as we do below.

Besides the coherence scale, we also require an estimate for the maximum available current to generate the magnetic fields. The current filaments are produced by the response of the

[8] If the returning electrons reach equipartition with the ions, as is the case for an electron-ion Weibel-mediated shock (Spitkovsky 2008b; Sironi et al. 2013), then one should strictly speaking use the combined density of beam ions *and* electrons to define the beam-plasma frequency (Lemoine & Pelletier 2011). In the pair-loaded case, beam electrons and positrons do not contribute to the upstream turbulence as much as the beam ions, because they carry on average lower relativistic inertia. For simplicity, we define here the beam-plasma frequency based on ions only.

[9] In a 2D geometry with an out-of-plane mean magnetic field, the appropriate adiabatic index for a relativistic gas is $\Gamma_{ad} = 3/2$.

background plasma to the return particle beam, which deposits a fraction of its energy into Weibel turbulence. Therefore, we identify the maximum current with the current of the return ion beam, $J_{\rm b} \simeq \xi_{\rm b} e n_{0{\rm i}} c$. Using Ampere's law based on the beam current, the maximum Weibel field strength is thus estimated as

$$\delta B \simeq 4\pi e \xi_{\rm b} n_{0{\rm i}}/k_{*}. \tag{12}$$

Based on Equations (8), (11), and (12), the near-upstream magnetic energy fraction and transverse coherence scale are obtained as

$$\epsilon_B \simeq \xi_{\rm b}^{5/3} \epsilon_{\rm e}^{2/3} (Z_{\pm}+1)^{-4/3}, \tag{13}$$

$$\lambda/d_{\rm i} \simeq \pi \xi_{\rm b}^{-1/6} \epsilon_{\rm e}^{1/3} (Z_{\pm}+1)^{-2/3}. \tag{14}$$

Compared to the symmetric case (Equation (9)) the scalings are modified through the addition of $\xi_{\rm b}$. In the near precursor of an electron-ion Weibel-mediated shock, typically $\xi_{\rm b} \approx 0.1$, $\epsilon_{\rm e} \approx 0.3$, $\epsilon_B \approx 0.01$, and $\lambda/d_{\rm i} \approx$ a few (e.g., Sironi et al. 2013). For $\xi_{\rm b} = 0.1$, $\epsilon_{\rm e} = 0.3$, and $Z_{\pm} = 0$, (13) and (14) give $\epsilon_B \approx 0.01$ and $\lambda/d_{\rm i} \approx 3$, consistent with previous simulations using electron-ion plasma compositions.

When comparing the simulation results to the scaling estimates (13) and (14), one should keep in mind that the scalings are obtained for a steady-state Weibel-mediated shock with $Z_{\pm} \ll m_{\rm i}/m_{\rm e}$. In principle, the most obvious choice would be to check the predictions in the absence of external magnetization, so that the shock is certainly Weibel mediated. However, as shown in Section 4.6, the structure of a pair-loaded shock in the $\sigma = 0$ limit differs substantially from the physics picture presented above and needs to be considered separately, owing to the creation of intense magnetic cavity structures. On the other hand, with increasing magnetization or pair loading the shock moves toward the Larmor mediated regime. For these reasons, the predictions (13) and (14) are best tested in simulations with a small but finite magnetization and for moderate pair-loading factors. This is done in Figure 6, which shows the profiles of ϵ_B and λ for $Z_{\pm} = 0$, 2 at $\sigma = 5 \times 10^{-6}$.

The simulations shown in Figure 6 have been evolved well over 2000 $\omega_{\rm pi}^{-1}$ in order to reach a steady state. To make trends clearer, the curves have been shifted with respect to the (ion) shock position $x_{\rm sh}(t)$ and time averaged over $\approx$150 $\omega_{\rm pi}^{-1}$. The location $x_{*} = 50\, d_{\rm i} + x_{\rm sh}$ (vertical dashed lines in bottom panels) is used as a proxy to determine the representative near-upstream values of $\epsilon_{\rm e}$ and $\xi_{\rm b}$ for use in Equations (13) and (14).[10] We compute $\xi_{\rm b}$ by identifying ions with $\beta_x > 0$ as the beam population. The profile of $\xi_{\rm b}$ is nearly independent of $Z_{\pm}$ in the near precursor, but decays more rapidly for $Z_{\pm} = 2$ at larger distances because the pair-loaded shock does not produce high-energy ions while the electron-ion shock does (see Section 5.2). The high-energy ion beam population of the $Z_{\pm} = 0$ shock travels further upstream and seeds the micro-turbulence at larger distances, leading to a more extended region of field growth and electron preheating, as evident from the profiles of $\epsilon_{\rm e}$.

The strength of the self-generated magnetic turbulence, as quantified by $\epsilon_B(x)$ in Figure 6, drops almost by an order in magnitude when the plasma is enriched with only a single pair per ion. Similarly, the transverse coherence scales $\lambda(x)$ become

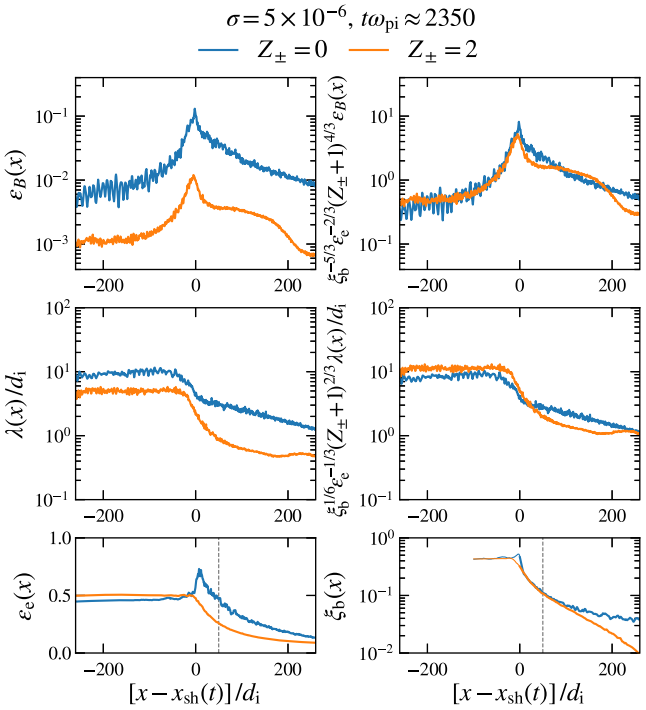

Figure 6. Profiles of the magnetic energy fraction $\epsilon_B(x)$ (top) and of the transverse field coherence scale $\lambda(x)$ (middle) for $Z_{\pm} = 0$, 2 at $\sigma = 5 \times 10^{-6}$. The profiles are shown with no rescaling on the left. On the right, we compensate the curves with the scaling predictions (13) and (14). The bottom panels show the pair energy fraction $\epsilon_{\rm e}(x)$ (left) and the beam parameter $\xi_{\rm b}(x)$ (right).

smaller. Immediately ahead of the shock and in the downstream, the compensation by the scaling predictions (13) and (14) nearly eliminates the difference between the results obtained for $Z_{\pm} = 0$ and $Z_{\pm} = 2$. This shows that the arguments presented above offer a sensible explanation for why the microturbulence weakens when the upstream is loaded with electron-positron pairs. A central feature of the model is the screening of ion currents by the hot pair background, which controls the coherence scale of the near-upstream Weibel filaments and leads to the weakening of the microturbulence with growing $Z_{\pm}$.

We stress that the above interpretation is appropriate in the regime $Z_{\pm} \ll m_{\rm i}/m_{\rm e}$ where the ions dominate the energy budget, since our estimates do not account for the fields generated from the free energy stored in pairs. Supposing that a fixed fraction of the far upstream pair kinetic energy is converted into electromagnetic fields, it may be reasonably expected that the magnetic energy actually increases with the pair-loading factor for $Z_{\pm} \gtrsim m_{\rm i}/m_{\rm e}$ when normalized to the fixed kinetic energy of the ions. Figure 3 provides a possible hint toward this regime, given that at $Z_{\pm} \geqslant 6$ the magnetic fields near the shock do not exhibit the sharp decline in strength seen at moderate pair-loading factors (in fact, the strength of B_z near the shock and in the upstream is somewhat higher for $Z_{\pm} = 12$ than it is for $Z_{\pm} = 6$).

4.4. Downstream Decay of the Magnetic Field

Up to this point, we have mainly focused on the evolution of magnetic turbulence in the near upstream of a pair-loaded shock. Downstream of the shock, the magnetic fluctuations

[10] We checked that the predicted value of $\epsilon_B(x)$ and $\lambda(x)$ is rather insensitive to the precise choice of the near-upstream location where $\epsilon_{\rm e}$ and $\xi_{\rm b}$ are measured.

appear nearly static in the frame of the shocked plasma and decay via phase mixing of the self-consistent electric currents. The results shown in Figure 6 (top panels) suggest that the magnetic field decay might be only moderately dependent on $Z_\pm$. Let us consider why this might be so.

For unmagnetized particles the linear damping rate of the fluctuations with wavenumber k is estimated as $\gamma_k \simeq (kc)^3/\tilde{\omega}_{\rm pe}^2$ (for details, see Chang et al. 2008; Lemoine 2015). Since the typical wavenumber of the fluctuations is comparable to k_*, it is instructive to evaluate γ_k for $k \sim k_*$. Using Equations (8) and (11), this gives

$$\gamma_{1/\lambda} \sim \omega_{\rm pi}(\omega_{\rm pi}/\tilde{\omega}_{\rm pe})^2(k_* d_{\rm i})^3 \sim \xi_{\rm b}^{1/2}\omega_{\rm pi}. \quad (15)$$

For simplicity, we have ignored the fact that k_* is estimated in the near precursor, whereas the damping rate concerns the downstream fluctuations. According to this crude estimate, the damping rate at the wavenumber k_* depends on $Z_\pm$ only implicitly via $\xi_{\rm b}$. Therefore, it seems possible that the overall rate of magnetic field decay is indeed only weakly dependent on $Z_\pm$ (as long as $\xi_{\rm b}$ does not change). A definite answer to this question requires simulations with $Z_\pm \gg 1$ evolved over several thousands of ion plasma times, which is computationally prohibitive at present. From a theoretical perspective, a more complete treatment would have to consider the evolution of the entire magnetic field spectrum and possible modifications of the damping due to particle trapping and nonthermal features in their energy distribution (Chang et al. 2008; Keshet et al. 2009; Lemoine 2015). We defer a detailed investigation of these aspects to future studies.

4.5. Critical Magnetization for a Larmor Mediated Shock

We have shown that, as the plasma is loaded with pairs, a weakly magnetized Weibel shock is transformed into one which is essentially Larmor mediated. From the simulations we can infer that the critical magnetization $\sigma_{\rm L}$, required for the ion shock to become Larmor mediated, roughly scales as $\sigma_{\rm L} \propto (Z_\pm + 1)^{-1}$. For $Z_\pm = 2$ and $Z_\pm = 0$ we find the transition near $\sigma_{\rm L} \approx 3 \times 10^{-5}$ and $\sigma_{\rm L} \approx 10^{-4}$ (not shown), respectively, the latter being consistent with earlier simulations of electron-ion shocks (e.g., Sironi et al. 2013). For $Z_\pm = 6$ we infer $\sigma_{\rm L} \approx 10^{-5}$ based on the shock structure shown in Figures 3 and 4.

To obtain a prediction for the scaling of $\sigma_{\rm L}$ one should determine when the motion of the background ions across the shock becomes dominated by the mean field as opposed to random scattering in the fluctuating fields. A tentative scaling broadly consistent with our simulations can be obtained by adopting the scattering frequency derived by Lemoine et al. (2019b), appropriate for particles that become trapped in the upstream Weibel filaments. The scattering frequency of the trapped background ions, normalized to their Larmor frequency in the mean field $\Omega_{\rm L0}$, is estimated as $\nu_{\rm scat}/\Omega_{\rm L0} \sim (\epsilon_B/\sigma)^{1/2}\lambda/\ell_\parallel$, where $\ell_\parallel$ is a characteristic longitudinal scale of the filaments (Lemoine et al. 2019b). The mean field dominates the transport when $\Omega_{\rm L0} \gtrsim \nu_{\rm scat}$. Using Equation (13), there follows the estimate

$$\sigma_{\rm L} \sim (\lambda/\ell_\parallel)^2\epsilon_B \sim (\lambda/\ell_\parallel)^2\xi_{\rm b}^{5/3}\epsilon_{\rm e}^{2/3}(Z_\pm + 1)^{-4/3}. \quad (16)$$

For typical values $\lambda/\ell_\parallel \approx 0.1$, $\xi_{\rm b} \approx 0.1$, $\epsilon_{\rm e} \approx 0.3$, this yields $\sigma_{\rm L} \sim 10^{-4} \times (Z_\pm + 1)^{-4/3}$, which is in reasonable agreement with our simulations. For reference, the ion Larmor radius in the rest frame of the upstream Weibel filaments ("Weibel frame," Pelletier et al. 2019) is $R_{\rm L,w}/d_{\rm i} \sim \epsilon_B^{-1/2}\gamma_{\rm w}\gamma_{\rm part,w}/\gamma_0$, where $\gamma_{\rm w}$ is the Lorentz factor of the Weibel frame (with respect to the downstream) and $\gamma_{\rm part,w}$ is a typical Lorentz factor of a particle in this frame. From Equations (12) and (14) it follows that $R_{\rm L,w}/\lambda \sim \pi^{-1}\xi_{\rm b}^{-2/3}\epsilon_{\rm e}^{-2/3}(Z_\pm + 1)^{4/3}\gamma_{\rm w}\gamma_{\rm part,w}/\gamma_0$. A reasonable choice of parameters ($\gamma_{\rm w}$ and $\gamma_{\rm part,w}$ both mildly relativistic, $\gamma_0 \approx 50$, $\xi_{\rm b} \approx 0.1$, and $\epsilon_{\rm e} \approx 0.3$) gives $R_{\rm L,w}/\lambda \sim (Z_\pm + 1)^{4/3}$. This implies that the near-upstream background ions are marginally trapped ($R_{\rm L,w} \sim \lambda$) in the Weibel filaments when the composition is electron-ion and become progressively less magnetized with growing $Z_\pm$. In practice, the trapping regime may as well extend up to $Z_\pm$ of a few, given that the ions are concentrated at the shock in small-scale density filaments, surrounded by locally intense fields with amplitudes above the typical fluctuation strength (see Figure 10).

If instead, the background ions are unmagnetized, the usual estimate for the critical magnetization gives $\sigma_{\rm L} \sim \epsilon_B^2(\lambda/d_{\rm i})^2$ (e.g., see Vanthieghem et al. 2020). Together with Equations (13) and (14), this translates into $\sigma_{\rm L} \sim 10^{-3} \times (Z_\pm + 1)^{-4}$ for typical values of $\xi_{\rm b}$ and $\epsilon_{\rm e}$. The latter is inconsistent with our numerical results for pair-loading factors of order unity, but may become relevant in high-$Z_\pm$ shocks with realistic ion-electron mass ratios, such that $1 \ll Z_\pm \ll m_{\rm i}/m_{\rm e}$; a regime currently inaccessible to long-duration PIC simulations.

It should be noted that the transport of the background plasma over the precursor of a pair-loaded shock warrants further investigation beyond the scope of the present work. One aspect worth mentioning concerns the slowdown of the background plasma under the influence of the perpendicular current driven instability (Lemoine et al. 2014), which is not considered in our scaling estimates, but may play an important role in bridging the gap between the Weibel and Larmor mediated shock regimes.[11]

4.6. Unmagnetized Limit

So far, we discussed the regime of small yet finite external magnetization, probing typical values of the order of $\sigma \sim 10^{-5}$. We showed that the self-generated microturbulence weakens as the plasma is loaded with pairs. As it turns out, this trend cannot be extrapolated to arbitrarily low σ because the unmagnetized limit exhibits features qualitatively different from the weakly magnetized case.

In Figure 7 we show the late-time structure of an unmagnetized shock with moderate pair loading.[12] In this case, the precursor is filled with intense magnetic structures with near equipartition fields strengths. The structures are born out of Weibel filaments, forming cavities in the background plasma density. These cavities are filled with intense magnetic fields (locally as high as $\epsilon_B \sim 1$), the amplitude of which shows no apparent dependence on $Z_\pm$.[13] As time progresses, the structures grow and merge, reaching scales up to several ion skin depths in size. In the long-time regime, the magnetic

[11] To our knowledge, the perpendicular current driven instability was so far studied only in weakly magnetized pair plasma shocks (Lemoine et al. 2014; Plotnikov et al. 2018). Its role in shocks with different particle compositions is not well understood at present.

[12] An animation showing the shock time evolution is available online at: https://youtu.be/vHnX1n-s90Y.

[13] More specifically, we also performed simulations for $\sigma = 0$ and $Z_\pm = 4$, 6 up to $t\omega_{\rm pi} \approx 1500$ and found no clear dependence of the local cavity field amplitude on $Z_\pm$.

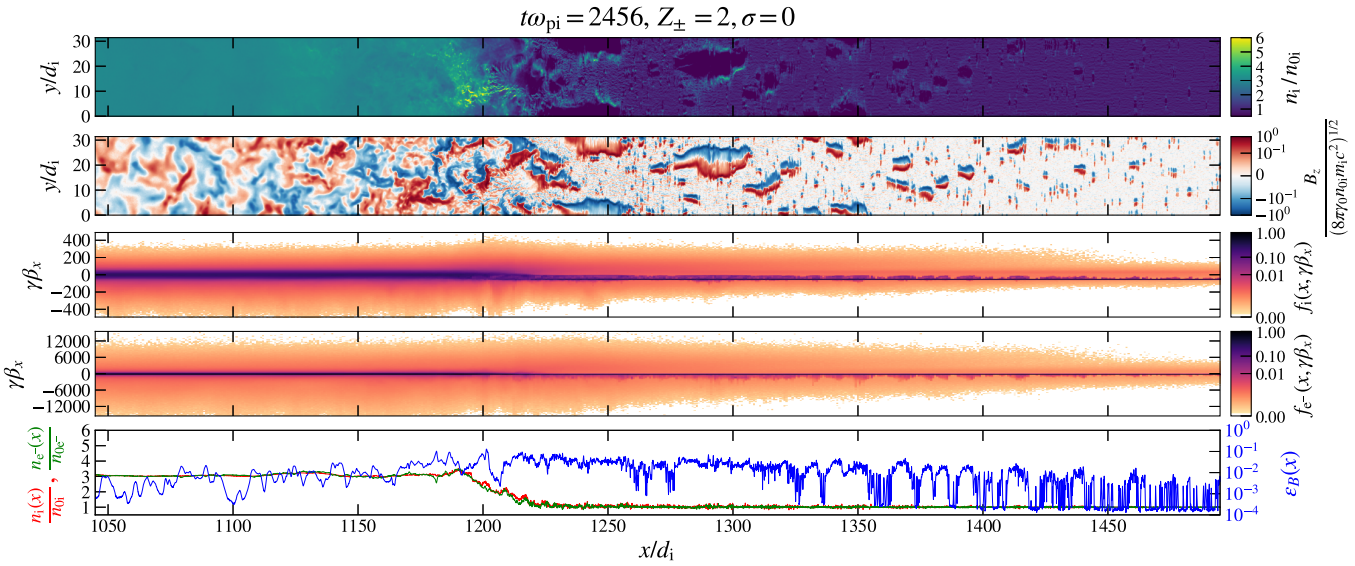

Figure 7. Late-time structure of a pair-loaded shock in the absence of external magnetization ($\sigma = 0$). Shown from top to bottom are the ion density, the out-of-plane magnetic field, the longitudinal ion and electron phase space, and the y-averaged particle density and magnetic energy fraction.

cavities penetrate toward the near precursor and build up an intense magnetic barrier at the shock with a mean magnetic energy fraction of the order of $\langle \epsilon_B \rangle \sim 0.1$. As the particles scatter off the intense magnetic fields, their nonthermal acceleration becomes more efficient (see Section 5.2). The limit of an unmagnetized pair-loaded shock is therefore different from the weakly magnetized regime, in the sense that a moderate pair enrichment does not lead to a reduced efficiency of particle scattering.

Similar structures have been previously observed in a variety of streaming unstable configurations, ranging from precursors of relativistic electron-ion shocks (Naseri et al. 2018) to simulations of laser-plasma experiments (e.g., Honda et al. 2000), including laser-driven shocks (Fiuza et al. 2012; Ruyer et al. 2015a). More recently, the magnetic cavities were analyzed in simulations of relativistic beam-plasma instabilities (Bresci et al. 2021; Peterson et al. 2021, 2022). These authors showed that the growth of magnetic cavities is essentially driven by the relativistic beam electrons, streaming over an electron-ion or electron-ion-positron background. In particular, Peterson et al. (2021) interpret the growth of the magnetic cavities as a secondary nonlinear instability of Weibel filaments. In their model, the secondary instability saturates either when the beam electrons become trapped in the cavity or when the background ions are accelerated in the upstream rest frame to relativistic velocities, such that they neutralize the electron beam current. The high Lorentz factor of our simulated shock ($\gamma_0 = 50$) ensures that the relativistic inertia of the beam electrons exceeds $m_i c$ ($= 36\, m_e c$) in the upstream frame, and therefore the background ions neutralize the current of the beam electrons before the latter become trapped. In our notation, the saturation strength obtained by Peterson et al. (2021) then becomes $\epsilon_B = \delta B^2/8\pi n_{0i}\gamma_0 m_i c^2 \sim \alpha_u$, where α_u is the ratio between the beam electron and background ion density, measured in the upstream frame of the background ions. In the far precursor $\alpha_u \ll 1$, but the ratio α_u grows as the upstream plasma is advected closer to the shock and experiences a growing electron beam density. In the simulation shown in Figure 7, the fields reach $\epsilon_B \sim 1$ locally at the cavity, implying that effectively $\alpha_u \sim 1$ where the amplitude saturates.

In our present understanding, the key feature that enables the generation of equipartition field strengths is the fact that the background plasma is evacuated from the cavity. As a result, the screening effect that otherwise limits the field growth (see Sections 3 and 4.3) is inhibited, because there are hardly any background particles left to screen the current inside the cavity.

In the simulation depicted in Figure 7, the structure of the shock is still evolving even at relatively late times. This naturally prompts the question about the ultimate fate of the magnetic cavities in the long time limit. Given that the structures always appear with the same magnetic field polarity, it is evident that an asymmetry in the inertia of the different species is a necessary condition for the cavity generation (Bresci et al. 2021; Peterson et al. 2022). Such asymmetry is naturally present in a pair-loaded shock, both for the incoming as well as the returning beam particles. For the latter, we remind that the pairs are heated below energy equipartition with the ions when $Z_{\pm} \gtrsim 1$ (see Section 5.1). Whether this is in fact a sufficient condition for sustained cavity generation should be investigated further.

It should be mentioned that we observe the cavities also in our electron-ion shock simulations, as well as in pair-loaded shocks with a low but finite $\sigma \lesssim 3 \times 10^{-5}$. The key difference from the simulations for $\sigma = 0$ is that the cavities are rather transient in nature. At finite magnetizations, the cavities appear at relatively early times, following the initial reflection of plasma from the simulation wall, and typically remain confined to within the far upstream without growing to large size. After this initial transient, the simulations at finite values of σ approach a steady state, apparently free from the magnetic cavities. In electron-ion simulations at $\sigma = 0$, we as well observe fewer cavities, but larger in size, as time progresses (see also Naseri et al. 2018). This could potentially indicate that the near energy equipartition between the returning beam electrons and ions is limiting the cavity production. On the other hand, the evolution of the structures in our electron-ion $\sigma = 0$ simulations might be as well affected by numerical limitations (e.g., the production of the cavities could be constrained by the limited width of the simulation box).

Additional numerical experiments, beyond the scope of this work, are needed to clarify this aspect.

4.7. Range of Applicability of the Unmagnetized Limit

We showed that the limit of an unmagnetized pair-loaded shock differs from the regime of weak but finite external magnetization. It is worth asking how low should σ be for the shock to be considered unmagnetized. A common criterion found in the literature is based on the requirement that the upstream residence time of the returning beam particles is controlled by scattering in the self-generated fields, rather than by the gyration in the mean upstream magnetic field. This amounts to $\sigma \lesssim \sigma_{\rm um} \sim \gamma_{\rm p}^{-2}\epsilon_B^2(\lambda/d_{\rm i})^2$ for beam particles with typical energy $E \sim \gamma_0 m_{\rm i}c^2$, where $\gamma_{\rm p}$ is the Lorentz factor of the incoming background plasma in the downstream frame (e.g., see Lemoine & Pelletier 2010; Lemoine et al. 2014).[14] Assuming that, regardless of $\gamma_0 \gg 1$, the background plasma decelerates from the far precursor to a typical bulk Lorentz factor $\gamma_{\rm p} \sim 10$, and that owing to the magnetic cavity generation we have on average $\epsilon_B \sim 0.01$ and $\lambda \sim d_{\rm i}$, we obtain $\sigma \lesssim \sigma_{\rm um} \sim 10^{-6}$. This upper limit is consistent with our simulations, showing explicitly that magnetizations as low as $\sigma \approx 5\times10^{-6}$ are too high for the shock to be considered unmagnetized. In our present understanding, it is even more likely that the unmagnetized limit requires $\sigma \ll 10^{-6}$. Moreover, it is possible that $\sigma_{\rm um}$ depends on $Z_\pm$. Very long-duration simulations at extremely low but finite $\sigma \lesssim 10^{-6}$ are required to further constrain this critical value.

5. Energy Partitioning and Particle Acceleration

So far, we focused on the kinetic-scale structure of a relativistic shock enriched with electron-positron pairs. Now, we discuss how the shock redistributes the incoming kinetic energy among the ions and pairs in the post-shock plasma.

5.1. Pair Energy Fraction

For accurate modeling of the radiation emission, it is important to determine what fraction of energy is drawn from the ion reservoir and transferred to the pairs during their passage across the shock. We quantify this energy exchange with the pair energy fraction $\epsilon_{\rm e} = (Z_\pm + 1)\overline{\gamma}_{\rm e} m_{\rm e}/\gamma_0 m_{\rm i}$, which we measure downstream of the shock (Figure 8). The measurements are obtained in a slab between -150 and $-100\,d_{\rm i}$ behind the ion shock, around the time $t\omega_{\rm pi} \approx 1650$. Quantitatively similar results are obtained at later times. As shown in Figure 8, the pair energy fraction is robustly in the range between 20% and 50% over the entire range of magnetizations considered. Higher magnetizations (comparable to $\sigma \sim 10^{-4}$) yield somewhat lower pair energy fractions, around 20%, compared to the lowest σ range with $\sigma \lesssim 10^{-5}$, where the values of $\epsilon_{\rm e}$ are scattered around 40%.

The mean energy per particle, $\overline{E}_{\rm e} = \overline{\gamma}_{\rm e} m_{\rm e}c^2$, is obtained directly from the definition of $\epsilon_{\rm e}$ as

$$\overline{E}_{\rm e} = \epsilon_{\rm e}(Z_\pm + 1)^{-1}E_{0\rm i}, \tag{17}$$

[14] In contrast to the estimates for $\sigma_{\rm L}$ (Section 4.5), which concern the near-upstream incoming background ions, the expression for $\sigma_{\rm um}$ applies to the returning beam particles ahead of the shock (this brings in the $\gamma_{\rm p}^{-2}$ factor, see Lemoine & Pelletier 2010; Lemoine et al. 2014).

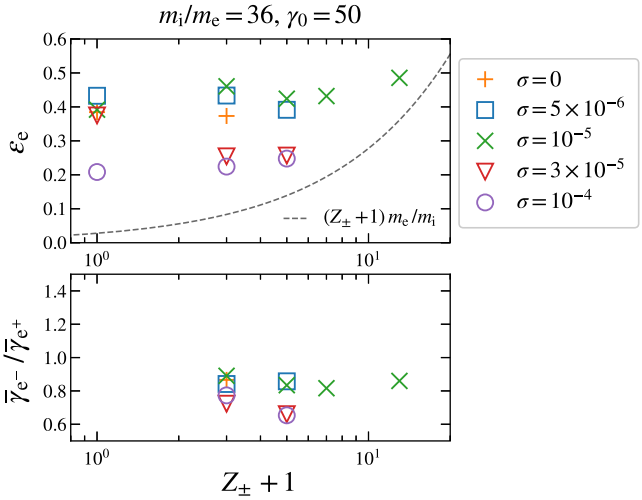

Figure 8. Downstream pair energy fraction (top) and the electron-positron mean energy ratio (bottom). The dashed curve in the top panel indicates the far upstream energy content of the pairs.

with $0.2 \lesssim \epsilon_{\rm e} \lesssim 0.5$ and $E_{0\rm i} = \gamma_0 m_{\rm i}c^2$. Therefore, with increasing $Z_\pm$ the post-shock pairs become cooler. Their mean energy scales approximately as $\overline{E}_{\rm e} \propto (Z_\pm + 1)^{-1}$. Apart from the pair energy fraction, we also determine the electron-positron energy ratio (Figure 8, bottom panel), which lies between 60% and 90%, regardless of the precise value of $Z_\pm$.

It is worth elaborating further on the physics of the electron and positron heating. In Figure 9 we show the mean work done by the electric field on a set of tracked particles (ions, electrons, and positrons) at $\sigma = 5\times10^{-6}$ for $Z_\pm = 0$, 2 from the far upstream, across the shock and into the downstream. We calculate separately the work done by the longitudinal (E_x) and transverse (E_y) electric field. Although the post-shock electrons are heated to nearly the same temperature as the positrons, we find that the positrons gain most of their energy by interacting with the shock-parallel E_x field, whereas the electrons primarily receive energy from the transverse E_y field. The ions lose energy through the interaction with both E_x and E_y. It is also interesting that most of the energization for $Z_\pm = 2$ occurs relatively close to the shock (within a distance of about 50 $d_{\rm i}$), compared to the electron-ion case.

The different mechanisms of electron and positron heating are related to strong ion density inhomogeneities near the shock transition. As shown in Figure 10, the ions near the shock transition form small-scale density structures with intense fluctuations around the mean. The electrons are drawn toward these structures as they try to compensate the ion space charge, but their density fluctuations appear more diffuse due to thermal effects. The positrons, on the other hand, are repelled away from the most intense ion density fluctuations. The E_x and E_y electric fields (bottom two panels in Figure 10) are correlated with the ion density inhomogeneities, and therefore the electrons receive the work by the electric field in a qualitatively different way than the positrons.

5.2. Particle Acceleration

Previous works have shown that relativistic shocks propagating into an electron-ion or electron-positron medium give rise to efficient particle acceleration via the first-order Fermi process (Achterberg et al. 2001), provided that the external

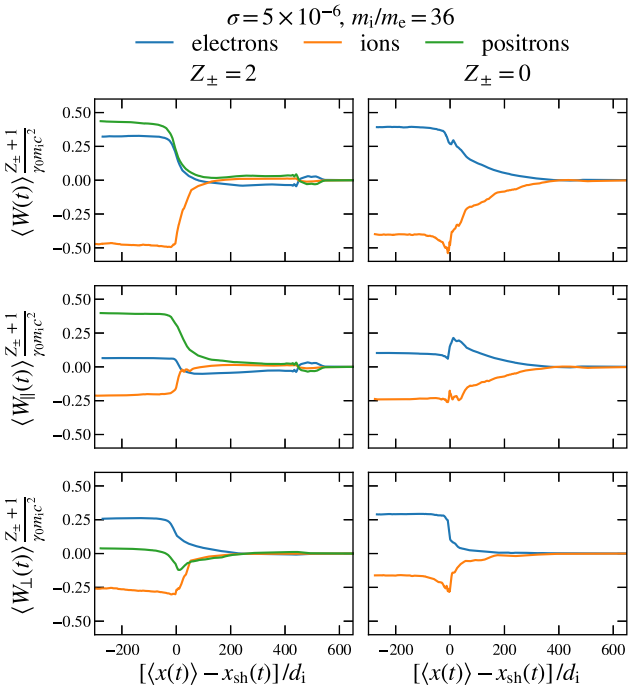

Figure 9. Work by the electric field on a tracked set of background particles as they stream toward and across the shock. Shown from top to bottom are the total work $W(t) = q\int \boldsymbol{E}(t)\cdot\boldsymbol{v}(t)dt$, the work due to the longitudinal $W_\parallel(t) = q\int E_x(t)v_x(t)dt$, and transverse field $W_\perp(t) = q\int E_y(t)v_y(t)dt$.

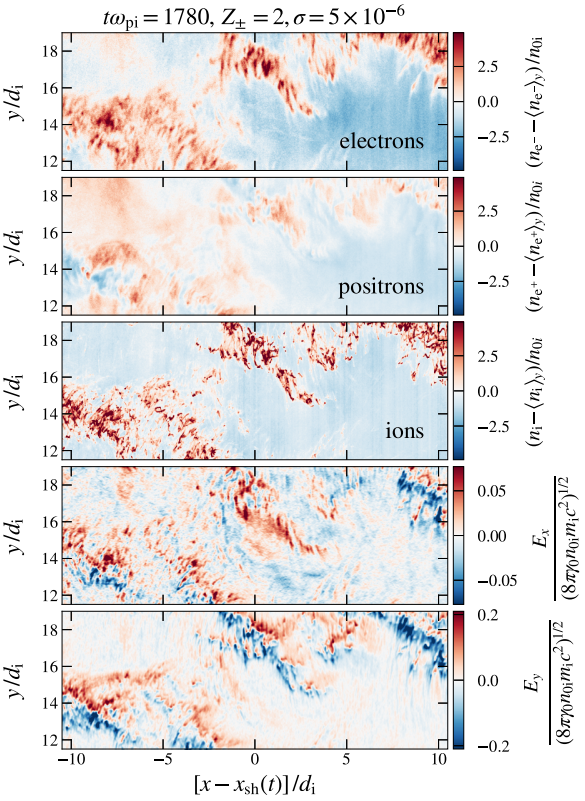

Figure 10. Small-scale structure of the shock transition region in a moderately pair-loaded plasma ($Z_\pm = 2$). Shown are the particle density fluctuations around the mean (top three panels) and the electric fields (bottom two panels).

magnetization is sufficiently weak (Spitkovsky 2008a; Martins et al. 2009; Sironi et al. 2013; Plotnikov et al. 2018). This maximum magnetization is determined by the requirement that the particle scattering in the microturbulence beats the motion in the compressed mean magnetic field that tries to advect the particles away from the shock toward the downstream (Pelletier et al. 2009). Let us consider the implications of the argument for a pair-loaded relativistic shock.

As appropriate for Fermi acceleration, we shall consider small-angle random scatterings of untrapped particles with $R_L \gtrsim \lambda$, where $R_L \simeq E/e\delta B$ is the Larmor radius of a particle with energy E in the fluctuating field δB. In the near downstream, a crude estimate based on Equations (12) and (14) gives $R_L/\lambda \sim (1/3)\pi^{-1}\xi_b^{-2/3}\epsilon_e^{-2/3}(Z_\pm+1)^{4/3}(E/\overline{E}_i)$, when the energy E is compared to the mean of the ion distribution $\overline{E}_i \sim E_{0i}$, and $R_L/\lambda \sim (1/3)\pi^{-1}\xi_b^{-2/3}\epsilon_e^{1/3}(Z_\pm+1)^{1/3}(E/\overline{E}_e)$ if the mean electron energy $\overline{E}_e$ is used instead.[15] Assuming $\xi_b \approx 0.1$ and $\epsilon_e \approx 0.3$, we find that the suprathermal ions and electrons with energies exceeding the mean (for each species) by factors of a few are always unmagnetized ($R_L \gtrsim \lambda$), and even more so at higher $Z_\pm$.

For the unmagnetized suprathermal particles, the downstream scattering frequency is estimated as $\nu_{scat} \simeq \lambda c/R_L^2$ (e.g., Plotnikov et al. 2011). Scattering prevails when $\nu_{scat} \gtrsim \Omega_{L0} \simeq eB_0c/E$, thereby enabling the particle to return to the shock instead of being advected further downstream by the mean field (Pelletier et al. 2009). The latter condition can be conveniently written as

$$\sigma \lesssim \sigma_F \simeq \epsilon_B^2(\lambda/d_i)^2(E/E_{0i})^{-2}, \tag{18}$$

where $E_{0i} = \gamma_0 m_i c^2$.[16] Here, we point out two important aspects. First, through the dependence of ϵ_B and λ on $Z_\pm$ (see Section 4.3), the maximum external magnetization that allows for Fermi acceleration becomes a function of the pair-loading factor. And second, if the electrons (and positrons) do *not* reach equipartition with the ions, as is generically the case for $Z_\pm \gtrsim 1$, then the condition for electron Fermi cycles is different from the one for the ions. In particular, condition (18) becomes less restrictive for the relatively cooler electrons near the thermal peak due to the inverse square dependence of σ_F on E, as long as this energy is high enough for a particle to remain untrapped (see discussion above).

Using Equations (13) and (14), the condition (18) can be expressed for ions as

$$\sigma \lesssim \sigma_{Fi} \simeq \pi^2\xi_b^3\epsilon_e^2(Z_\pm+1)^{-4}(E/\overline{E}_i)^{-2}, \tag{19}$$

where $\overline{E}_i \sim E_{0i}$. Taking typical values $\xi_b \approx 0.1$ and $\epsilon_e \approx 0.3$, we find that nonthermal ions with energies E exceeding the mean by a few can be produced when $\sigma \lesssim \sigma_{Fi} \sim 10^{-4}\times(Z_\pm+1)^{-4}$. On the other hand, for electrons we obtain

$$\sigma \lesssim \sigma_{Fe} \simeq \pi^2\xi_b^3(Z_\pm+1)^{-2}(E/\overline{E}_e)^{-2}, \tag{20}$$

[15] The factor of 1/3 accounts for the magnetic field compression at the 2D relativistic shock.

[16] The estimate (18) is similar to the one used in Section 4.5 to obtain σ_L for unmagnetized ions, but the question being asked is different. Here, we consider the near-downstream motion of the (nearly) isotropic suprathermal particle population, whereas Section 4.5 concerns the transport of the incoming background ions with typical energy $E \sim E_{0i}$ over the near precursor. We point out that the transport of the incoming background particles need not be, and generally is not, of the same nature as the transport of the suprathermal particle population (e.g., the background particles may be trapped in the Weibel filaments while the suprathermal population is not).

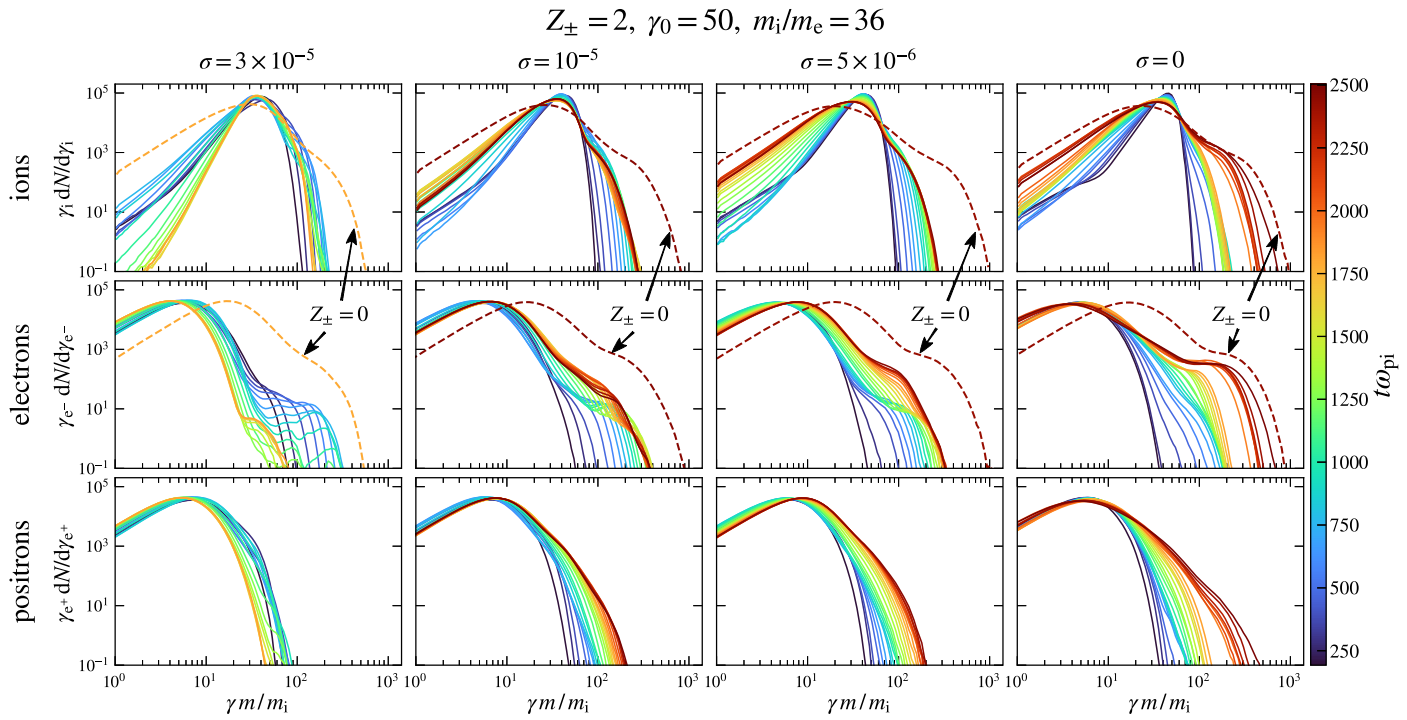

Figure 11. Energy spectrum evolution at fixed $Z_\pm = 2$ and for various magnetizations σ in a slab between -150 and $-100\,d_i$ behind the ion shock. Different colors are used to represent the simulation time. Dashed curves show the late-time spectra from electron-ion simulations ($Z_\pm = 0$).

with $\overline{E}_e \sim \epsilon_e (Z_\pm + 1)^{-1} E_{0i}$. Taking electrons with energy $E \approx 3\overline{E}_e/\varepsilon_e$, we estimate $\sigma_{Fe} \sim 10^{-4} \times (Z_\pm + 1)^{-2}$.

Based on the above, we envision a situation where nonthermal ion acceleration at the weakly magnetized shock is suppressed for $Z_\pm \gtrsim 1$, unless σ is extremely low, such that $\sigma \lesssim \sigma_{Fi}$. For electrons, limited acceleration remains possible as long as $\sigma \lesssim \sigma_{Fe}$, even when the ions are thermal. However, as soon as an electron is accelerated to energies of the order of $E \sim E_{0i}$, the nature of its transport becomes similar to that of the thermal ions, implying that any nonthermal acceleration beyond $E \sim E_{0i}$ is inhibited. Therefore, the electrons may form a nonthermal component even when the ions are essentially thermal, but the extent of the nonthermal tail will be in this case limited between $E \sim (Z_\pm + 1)^{-1} E_{0i}$ and $E \sim E_{0i}$. Finally, following the simplified physics picture discussed above, we expect electrons to be thermal when $\sigma \gtrsim \sigma_{Fe}$ (although, see Figure 14).

We now compare the above estimates with results from PIC simulations. Figure 11 shows the evolution of the downstream particle energy spectrum at fixed $Z_\pm = 2$ and for different magnetizations σ. The results shown represent some of our longest-duration simulations (in ω_{pi}^{-1} units) and are as such best suited for probing the nature of particle acceleration. At the time when each $Z_\pm = 2$ simulation ends, we also show the spectra obtained for $Z_\pm = 0$ at the same time. In line with the above discussion, we find that even a single electron-positron pair per ion is enough to suppress ion acceleration at magnetizations as low as $\sigma = 5 \times 10^{-6}$. In contrast, the electron-ion shock produces nonthermal ions up to $\sigma = 3 \times 10^{-5}$ (see also Sironi et al. 2013). These results are consistent with the estimate (19), which gives $\sigma_{Fi} \approx 10^{-4}$, 10^{-6} for $Z_\pm = 0$, 2, respectively. For electrons, condition (20) gives $\sigma_{Fe} \approx 10^{-5}$ at $Z_\pm = 2$, and indeed we observe the development of a limited nonthermal electron tail in simulations with $\sigma = 10^{-5}$, 5×10^{-6} at $Z_\pm = 2$. For $\sigma = 3 \times 10^{-5}$, the nonthermal electron component (except for a minor kink in the spectrum) is only a transient, connected to the initial reflection of particles from the wall on the left of the simulation domain (see also the discussion of Figure 14 in this section).

Unlike in the regimes with weak but finite σ, both ions and electrons form distinctly nonthermal distributions in the limit of vanishing σ (Figure 11, rightmost panels). The acceleration is intermittent in time and correlated with the formation of the magnetic cavities (see Section 4.6). To demonstrate the point, we show in Figure 12 the evolution of the maximum particle energy (i.e., the spectral cutoff) behind the shock together with the maximum of the y-averaged magnetic energy fraction, measured in a slab around the shock. Around the time $t\omega_{pi} \approx 1700$, when the first large-scale cavities appear in the near precursor, the magnetic energy fraction at the shock is amplified by an order of magnitude, followed by rapid growth of the maximum particle energy. At select times, the maximum energy grows at a rate considerably faster than $\max(\gamma) \sim (t\omega_{pi})^{1/2}$, previously reported for electron-ion and pair plasma compositions (Sironi et al. 2013; Plotnikov et al. 2018). While the observed trend is intriguing, we note that longer duration simulations are required for a reliable extrapolation to astrophysically relevant timescales.

The results of PIC simulations shown in Figure 11 reveal also a strong asymmetry between the electron and positron energy spectra. The highest energy electrons are accelerated to near equipartition with the highest energy ions, whereas the positrons are not. Moreover, the nonthermal component of the electron spectrum is much harder. To explain the origin of the asymmetry, we consider in Figure 13 the work by the E_x and E_y electric fields on a few representative high-energy electrons and positrons, extracted from the simulation with $\sigma = 5 \times 10^{-6}$ and $Z_\pm = 2$. The work by the shock-perpendicular E_y field is qualitatively similar for the two species and exhibits random kicks in the particle energy that are characteristic of diffusive

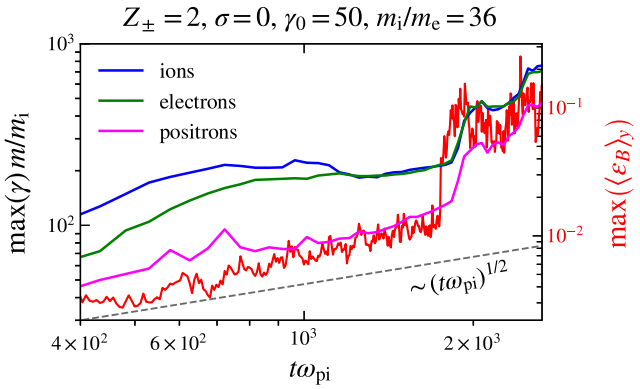

Figure 12. The maximum particle energy and magnetic energy fraction vs. time in a $\sigma = 0$ shock with moderate pair-loading factor. We determine $\max(\gamma)$ based on where $\gamma dN/d\gamma = 0.1$ in the selected units of Figure 11. The maximum of $\langle \epsilon_B \rangle_y$ is measured at the shock in a 50 d_i wide slab. The scaling $\sim (t\omega_{pi})^{1/2}$ is shown for reference only.

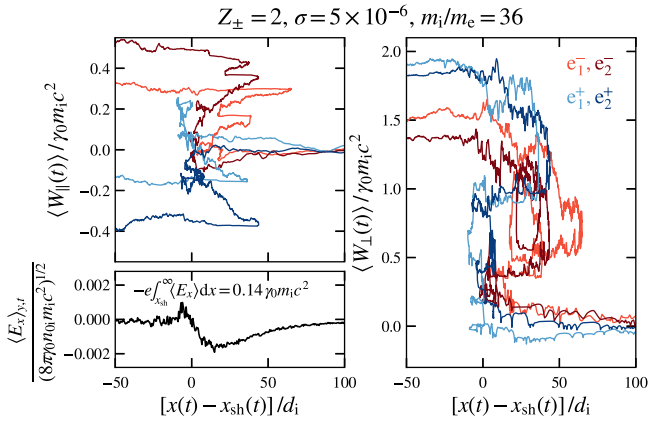

Figure 13. Work by the longitudinal (E_x) and transverse (E_y) electric field on a few high-energy positrons (blue lines) and electrons (red lines). The bottom left panel shows the mean profile of $E_x(x - x_{sh}(t), y, t)$, averaged over y and t (time interval matches the duration of particle tracking, $\Delta t\omega_{pi} \approx 1000$).

shock acceleration. On the other hand, the work by E_x is largely mediated by a coherent field component (Figure 13, bottom left panel) that points toward the shock in the near upstream, within a distance of about $\sim 50\, d_i$ ahead of the shock.

On each cycle between the upstream and downstream, the returning electrons interacting with E_x increase their energy by roughly $\Delta E/E_{0i} \sim 0.1$, while the positrons lose an equivalent amount. This value is consistent with the estimated drop of the electric potential from the shock toward the far upstream, which gives $e\int_{x_{sh}}^{\infty} \langle E_x \rangle dx \approx -0.14\, E_{0i}$. The return of the particle from the upstream back to the shock plays little role in this energy exchange because most of the upstream residence time is spent by the particle moving away from the shock; when the particle turns around it is caught up by the shock rapidly. Thus, the energy difference in the work done by E_x accumulates upon repeated cycles, thereby favoring electron over positron acceleration. In the presence of magnetic cavities, some of the incoming background electrons (but not positrons) are preaccelerated near the cavities (see the longitudinal electron phase space in Figure 7), which promotes the asymmetry further.

It is worth commenting on how the coherent E_x field that favors electron over positron acceleration is generated. This field can be attributed to the fact that the returning beam ions carry on average higher relativistic inertia than the pairs, and therefore they penetrate further into the upstream, leaving behind most of the electrons and positrons with an excess negative charge. The resulting electrostatic potential gives rise to a near-upstream electric field that points in the negative x direction. It should be mentioned that this coherent field is much smaller than the fluctuating fields near the shock transition (see Figure 10). However, because it systematically affects the electron and positron energy gain on each Fermi cycle it leads to an overall significant difference between the nonthermal spectra of electrons and positrons.

For reference, we show in Figure 14 the downstream energy spectrum evolution at fixed $\sigma = 10^{-5}$ and for various $Z_\pm$. We caution the reader that beyond $Z_\pm$ of a few finite mass ratio effects for our choice of $m_i/m_e = 36$ are not to be ruled out (see Appendix A). With this caveat in mind, we report the following. Except when $Z_\pm = 0$, the ions are essentially thermal, lacking any substantial nonthermal component. The relatively cooler electrons with mean energy $\overline{E}_e = \epsilon_e (Z_\pm + 1)^{-1} E_{0i}$ develop a limited nonthermal tail with a cutoff energy $E \sim (Z_\pm + 1)^{-1} E_{0i}$. The acceleration of positrons is disfavored by the mean electric field in front of the shock (see the discussion above), such that the positrons remain nearly thermal. The electron spectrum features as well a high-energy spectral bump that gradually recedes with time. Particle tracking (not shown) relates the high-energy bump with a transient energization of electrons near the tip of the particle precursor. The feature is therefore a remnant of the initial reflection of plasma from the simulation wall, and does not persist in the long-time regime of particle acceleration. To summarize, the generic property that emerges from our simulations of weakly magnetized pair-loaded shocks is that the ions are essentially thermal, whereas the electrons form a nonthermal tail of limited extent.

For $Z_\pm \geqslant 4$, the magnetization of $\sigma = 10^{-5}$ is above the estimated range of σ (see Equation (20)) that allows for electron Fermi cycles. An important aspect to consider here is that for high $Z_\pm$ the electron shock lies ahead of the broader ion shock (Figure 4), and the space in between is filled with a turbulent field sheared by a transverse $E_x \times B_z$ flow (see the discussion of Figure 5 in Section 4.2). This feature departs from the context in which the estimate (20) is made, where the particle scattering centers behind the shock are essentially at rest in the downstream frame. That significant electron energization indeed occurs behind their shock can be seen by inspecting the spectrum at different x locations, as shown in Figure 15. The electron spectrum immediately behind the electron-positron shock exhibits a much softer nonthermal component compared to the far downstream spectrum, behind the broader ion shock. Moreover, not only the high-energy component, but also the core of the particle distribution is energized during the passage through the turbulent sheared layer in between the two shocks.

6. Astrophysical Implications

The results presented in this paper are relevant for the early phase of the GRB afterglow, when the external shock propagates into a medium enriched with electron-positron pairs. We provide direct estimates for the fraction of energy carried by the post-shock pairs and constrain the maximum external magnetization that allows for efficient particle acceleration.

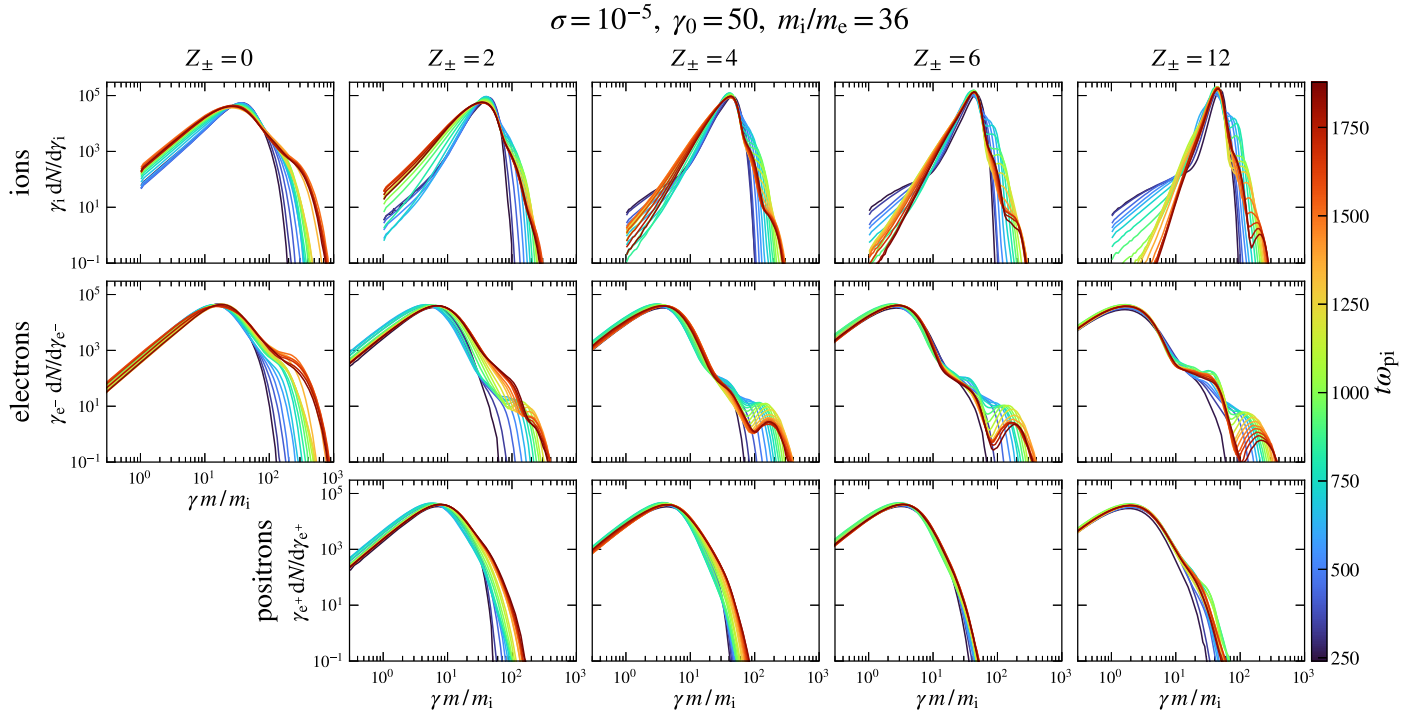

Figure 14. Energy spectrum evolution at fixed $\sigma = 10^{-5}$ and for increasing $Z_\pm$ (left to right) in a slab between -150 and $-100\,d_i$ behind the ion shock.

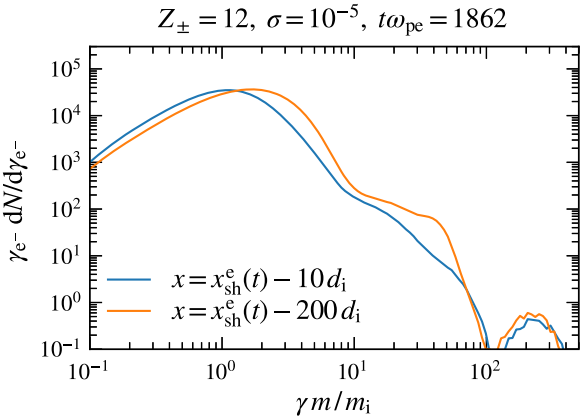

Figure 15. Electron spectrum in a 10 d_i wide slab at two different x locations behind the pair shock for $Z_\pm = 12$ and $\sigma = 10^{-5}$.

GRB explosions may occur in the interstellar medium or inside the wind of a massive progenitor star, in particular of Wolf-Rayet type (Crowther 2007). The magnetization of the interstellar medium is extremely low; it varies around $\sigma \sim 10^{-9}$. The magnetization of a Wolf-Rayet wind before the explosion is likely much higher than the magnetization of the interstellar medium, but its exact value is poorly known. An upper limit may be estimated using the wind kinetic energy per particle. This gives $\sigma \lesssim (w/c)^2 \sim 10^{-5}$ for typical wind velocities $w \sim 10^8\,\mathrm{cm\,s^{-1}}$.

The model of the early GRB afterglow developed by Beloborodov et al. (2014) shows good agreement with a set of GRB observations, assuming ambient densities typical of Wolf-Rayet type progenitors and emission from essentially thermal pairs behind the shock, carrying an energy fraction $\epsilon_e \approx 0.3$ when $1 \lesssim Z_\pm \ll m_i/m_e$ (see also Hascoët et al. 2015). Our first-principles kinetic simulations support these assumptions. We find $0.2 \lesssim \epsilon_e \lesssim 0.5$ and rather limited nonthermal electron acceleration for magnetizations near the estimated upper limit of Wolf-Rayet stellar winds ($\sigma \sim 10^{-5}$). In this case, the maximum (downstream frame) energy of the nonthermal electrons is set by the shock Lorentz factor $\sim \gamma_0$ and the ion mass as $E \sim E_{0i} = \gamma_0 m_i c^2$. Efficient electron acceleration beyond $E \sim E_{0i}$ then requires either very small amounts of pair loading, expected at radii $R > R_\pm \sim 10^{17}$ cm (Beloborodov 2002), or extremely low magnetizations, such as those expected for the interstellar medium ($\sigma \sim 10^{-9}$).

7. Summary and Conclusions

In this work, we study the microphysics of pair-loaded, weakly magnetized relativistic shocks using 2D kinetic PIC simulations. Our simulations focus on the regime of moderate pair-loading factors $Z_\pm \lesssim 10$, where the far upstream energy is dominated by ions. We find the following:

1. Pair loading decreases the strength and scale of the self-generated turbulence over the weakly magnetized precursor, leading to a reduced efficiency of particle scattering. We attribute this effect to the screening of ion current filaments by the background pairs (Section 4.3).
2. When the external magnetization exceeds a critical value σ_L, the shock becomes mediated by the gyration of ions in the background compressed mean magnetic field (Sections 4.2 and 4.5). This critical value decreases with $Z_\pm$, owing to the weakening of the self-generated turbulence, which mediates the shock for $\sigma \lesssim \sigma_L$.
3. The energy fraction ϵ_e, carried by the post-shock pairs, is robustly in the range between 20% and 50% of the upstream ion energy (Section 5.1). These values are favored by models of the early GRB afterglow that account for the pair loading (e.g., Beloborodov et al. 2014; Hascoët et al. 2015). The mean electron energy

scales as $\overline{E}_e \simeq \epsilon_e (Z_\pm + 1)^{-1} E_{0i}$, where $0.2 \lesssim \epsilon_e \lesssim 0.5$ and $E_{0i} = \gamma_0 m_i c^2$ is the far upstream ion energy.

4. Pair loading limits nonthermal particle acceleration, most notably for ions (Section 5.2). We estimate that acceleration via the first-order Fermi process is possible only when the external magnetization is below a critical, pair-loading-dependent value $\sigma_F \sim 10^{-3} \times (Z_\pm + 1)^{-4} (E/E_{0i})^{-2}$, where E is the energy of the injected particle. Simulations indeed show that the ions are essentially thermal at magnetizations as low as $\sigma \approx 5 \times 10^{-6}$, even when the plasma is loaded with only single electron-positron pair per ion. The electrons, on the other hand, form a nonthermal component in the range between $E \sim (Z_\pm + 1)^{-1} E_{0i}$ and E_{0i}.
5. The limit of vanishing external magnetization is different from the regime with weak but finite σ (Section 4.6). When $\sigma = 0$, the microturbulence shows no apparent signs of weakening with growing $Z_\pm$; at least not for the order-unity values of $Z_\pm$ considered in our simulations. The locally intense fields are supplied by magnetized plasma cavities, generated over the turbulent precursor. Then, particle acceleration of both ions and electrons is sustained over the duration of the entire simulation. We estimate that, under the most favorable conditions, the external magnetization should be no larger than $\sigma \sim 10^{-6}$ for the pair-loaded shock to be an efficient accelerator of both electrons and ions (Section 4.7).

The subject offers a number of promising future directions. In our setup, the pair enrichment is characterized by a single parameter, the pair-loading factor $Z_\pm$, neglecting the fact that the pairs are injected with a finite momentum in the rest frame of the external medium. The available free energy of the drifting pairs is released through plasma streaming instabilities, which preamplify magnetic fields in the far upstream (Ramirez-Ruiz et al. 2007; Derishev & Piran 2016; Garasev & Derishev 2016; Peterson et al. 2022). If these fields manage to survive until they are caught up by the shock, the scale and strength of the fluctuations at the shock and further downstream could be modified. Pair enrichment also plays a significant role in relativistic radiation mediated shocks, although the physics in that case is somewhat different from the regime consider here, owing to direct momentum exchange between the radiation and the plasma (e.g., Levinson 2020; Vanthieghem et al. 2022). The present work motivates as well further studies along the lines of kinetic plasma theory. This includes, for instance, the theory for the slowdown of the background electrons and ions over the precursor of a pair-loaded shock, and the exact physical details required for the persistent generation of the magnetic cavities in low-σ pair-loaded relativistic shocks.

We thank I. Plotnikov, A. Philippov, J. Nättilä L. Comisso, J.R. Peterson, and A. Spitkovsky for helpful discussions related to this work. The authors would like to acknowledge the OSIRIS Consortium, consisting of UCLA and IST (Lisbon, Portugal), for the use of OSIRIS and for providing access to the OSIRIS 4.0 framework. D.G. was supported by the U.S. DOE Fusion Energy Sciences Postdoctoral Research Program administered by ORISE for the DOE. ORISE is managed by ORAU under DOE contract number DE-SC0014664. All opinions expressed in this paper are the authors' and do not necessarily reflect the policies and views of DOE, ORAU, or ORISE. L.S. acknowledges support by NSF grant No. AST-1716567 and NASA grant No. ATP 80NSSC20K0565. The authors acknowledge the Gauss Centre for Supercomputing e.V. for funding this project by providing computing time on SuperMUC-NG at the Leibniz Supercomputing Centre under project No. pr74vi (Principal Investigator: Jörg Büchner). Additional computing resources were also provided on NERSC Cori.

Software: OSIRIS (Fonseca et al. 2002, 2013).

Appendix A
Dependence on the Mass Ratio

In Figure 16 we compare the downstream particle energy spectra around the time $t\omega_{pi} \approx 815$ in a shock with $Z_\pm = 2$ and $\sigma = 5 \times 10^{-6}$ for $m_i/m_e = 36$, 100. To save resources, we perform the $m_i/m_e = 100$ simulation using a $17\, d_i$ wide box, with a resolution of 6.5 cells per d_e and four particles per cell per species. The $m_i/m_e = 36$ simulation has a $31.4\, d_i$ wide box, with a resolution of eight cells per d_e and 12 particles per cell per species.

As shown in Figure 16, qualitatively and quantitatively similar results are obtained at the increased value of the ion-electron mass ratio. We conclude that the simulations from the main text using $m_i/m_e = 36$ are reasonably converged in terms of the mass ratio for pair-loading factors up to a few. This is consistent with Sironi et al. (2013), who performed mass ratio scans (up to $m_i/m_e = 1600$) in simulations of relativistic electron-ion shocks at $\sigma = 10^{-5}$, and concluded that mass ratios as low as $m_i/m_e = 25$ are sufficient for reasonably converged results. It is also worth highlighting the excellent agreement in the thermal parts of the electron and positron spectra in Figure 16, even though the far upstream pair energy fraction, $\epsilon_{e0} = (Z_\pm + 1) m_e/m_i$, differs significantly between the two runs.

Computational limitations currently prevent long-duration shock simulations at mass ratios much higher than 36 for $Z_\pm$ beyond a few. However, the following can be noted. In Section 5.1 we demonstrate that the mean post-shock electron energy per particle drops as $\overline{E}_e \propto (Z_\pm + 1)^{-1}$ with the pair-loading factor. The trend ceases when $\overline{E}_e \approx \epsilon_e (Z_\pm + 1)^{-1} \gamma_0 m_i c^2 \approx \gamma_0 m_e c^2$, as the electrons get to keep their initial far upstream energy of $\gamma_0 m_e c^2$.

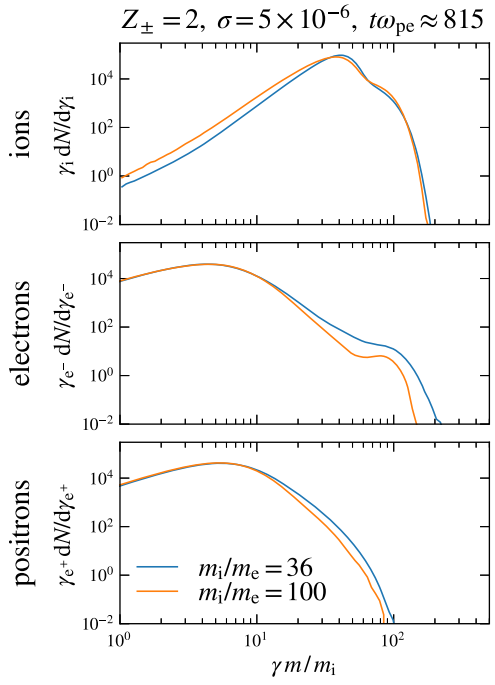

Figure 16. Dependence of the post-shock particle energy spectrum on the ion-electron mass ratio. The spectra are measured in a slab between -150 and $-100\, d_i$ behind the ion shock.

Therefore, mass ratio effects should become significant whenever $Z_\pm + 1 \sim \epsilon_e m_i/m_e$. This suggests that finite mass ratio effects could play a role in our simulations with $Z_\pm = 6$, 12 and $m_i/m_e = 36$. On the other hand, it is worth noting that our results are supported by analytical estimates, derived under the general assumption $Z_\pm \ll m_i/m_e$ and without specifying any particular value for m_i/m_e.

Appendix B
Mitigation of Numerical Cherenkov Instability

To mitigate the numerical Cherenkov instability we use a generalized stencil for the $\nabla \times \boldsymbol{E}$ derivative in Maxwell's equations (Blinne et al. 2018), which improves the numerical dispersion of electromagnetic waves and reduces the growth of the numerical instability. The $\nabla \times \boldsymbol{B}$ stencil is not modified so as to preserve the charge-conserving property of the current deposition algorithm. The coefficients of the generalized stencil are listed under the name "min. 3" in Table 1 of Blinne et al. (2018). For this particular stencil, the grid cells must be square and the time step should be set to $\Delta t = 0.5\,\Delta x/c$ for optimal results. Our approach provides an effective solution for avoiding the numerical Cherenkov instability in the low wavenumber range ($k \ll k_{\max} = \pi/\Delta x$), whereas at high wavenumbers the instability can be mitigated by low-pass filtering the electric currents at each time step, as is routinely done in relativistic PIC simulations (e.g., Spitkovsky 2005). Here, we employ a binomial filter with 20 passes in the longitudinal (x) and 10 in the transverse (y) direction.

In Figure 17 we demonstrate the performance of the Blinne et al. (2018) "min. 3" stencil in free streaming plasma simulations. The simulation domain is periodic with 2048^2 cells and 12 particles per cell per species. Other numerical parameters are reported in the figure. We initialize a uniform pair-loaded plasma streaming with a bulk Lorentz factor $\gamma_0 = 50$ in the x-direction and monitor the growth of the numerical Cherenkov instability. As shown in Figure 17, the modified stencil improves control over the numerical instability compared to the standard (Yee) field solver. A particularly strong suppression is obtained when the streaming plasma is initialized with a mild temperature ($T_0 = T_{0e} = T_{0i} = 8 \times 10^{-2}\, m_e c^2$). In that case, the numerical Cherenkov modes (seen in the $|k_x|d_e \gtrsim 6$, $|k_y|d_e \lesssim 1.5$ range of the B_z spectrum) remain limited to low amplitudes over the duration of the simulation. When the plasma is initially cold ($T_0 = 1.7 \times 10^{-3}\, m_e c^2$) numerical Cherenkov modes grow to an appreciable level in about 150,000 steps; a substantial improvement compared to results obtained using the standard Yee solver. With respect to shock simulations, we note that the time when the upstream becomes affected by spurious Cherenkov modes is delayed by roughly a factor of 4 (compared to the free streaming setup) when the upstream plasma is introduced gradually using a moving particle injector.[17] It is also worth mentioning that the incoming plasma acquires a mild temperature already at relatively large distances from the shock as a result of interaction with the counterstreaming beam of returning particles (e.g., Lemoine et al. 2019a). This may help reduce the growth of the numerical Cherenkov modes further.

[17] Approximating the instantaneous position of the shock and particle injector as $x_{sh} \approx ct/2$ and $x_{inj} \approx ct$ (downstream frame), respectively, it is easy to show that a patch of plasma streaming at speed $\approx -c$ reaches the shock at time step N if it was introduced via the particle injector roughly $\approx N/4$ steps earlier. Thus, the maximum time available to grow numerical Cherenkov modes (before the patch crosses the shock) is roughly a quarter of the total simulation time.

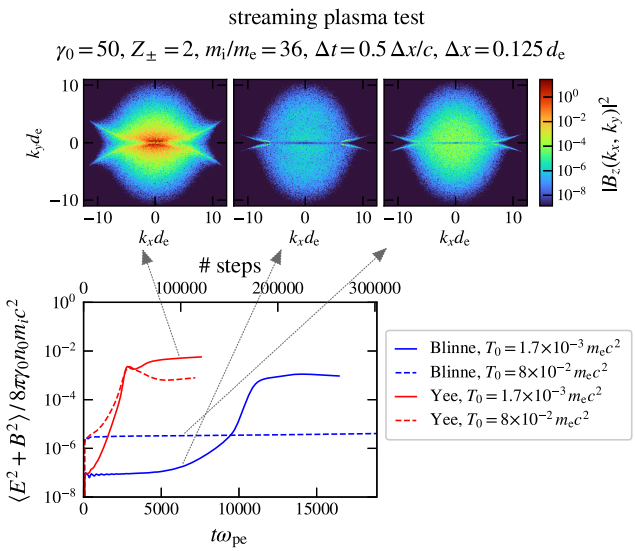

Figure 17. Evolution of the electromagnetic energy vs. time (bottom panel) in a free streaming plasma test. On top, we show the wavenumber spectra of B_z at 100,000 time steps for the three cases indicated by arrows.

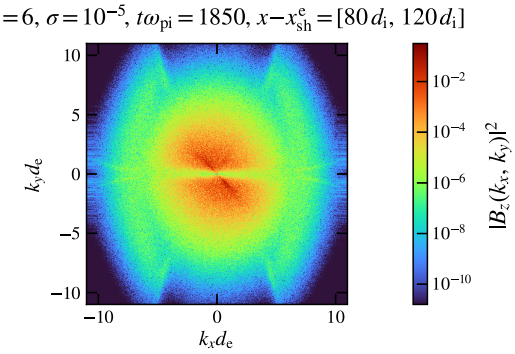

Figure 18. Wavenumber spectrum of B_z upstream of a pair-loaded shock at late time in the simulation.

In Figure 18 we show the spectrum of B_z in a slab between 80 and 120 d_i ahead of the (electron) shock from one of our longest simulations (in time step units) with $Z_\pm = 6$ and $\sigma = 10^{-5}$. The spectrum is shown at a time $t\omega_{pi} = 1850$ corresponding to 468,000 time steps in the simulation. As shown in Figure 18, the spectrum is dominated by relatively low wavenumber modes transverse to the shock normal. A careful look reveals a weak signature of Cherenkov modes in the same region of wavenumber space as in Figure 17 ($|k_x|d_e \gtrsim 6$, $|k_y|d_e \lesssim 1.5$), but their relative energy content is minor. We conclude that the numerical Cherenkov instability is controlled in our simulations to a sufficient degree that it does not significantly affect our results.

ORCID iDs

Daniel Grošelj https://orcid.org/0000-0002-5408-3046
Lorenzo Sironi https://orcid.org/0000-0002-1227-2754
Andrei M. Beloborodov https://orcid.org/0000-0001-5660-3175

References

Achterberg, A., Gallant, Y. A., Kirk, J. G., & Guthmann, A. W. 2001, MNRAS, 328, 393
Achterberg, A., & Wiersma, J. 2007, A&A, 475, 1
Achterberg, A., Wiersma, J., & Norman, C. A. 2007, A&A, 475, 19

Ackermann, M., Ajello, M., Asano, K., et al. 2013, ApJS, 209, 11
Amato, E., & Arons, J. 2006, ApJ, 653, 325
Beloborodov, A. M. 2002, ApJ, 565, 808
Beloborodov, A. M., Hascoët, R., & Vurm, I. 2014, ApJ, 788, 36
Blandford, R., & Eichler, D. 1987, PhR, 154, 1
Blinne, A., Schinkel, D., Kuschel, S., et al. 2018, CoPhC, 224, 273
Bresci, V., Gremillet, L., & Lemoine, M. 2022, PhRvE, 105, 035202
Bret, A., Stockem, A., Narayan, R., & Silva, L. O. 2014, PhPl, 21, 072301
Chang, P., Spitkovsky, A., & Arons, J. 2008, ApJ, 674, 378
Crowther, P. A. 2007, ARA&A, 45, 177
Davidson, R. C., Hammer, D. A., Haber, I., & Wagner, C. E. 1972, PhFl, 15, 317
Derishev, E. V., & Piran, T. 2016, MNRAS, 460, 2036
Fiuza, F., Fonseca, R. A., Tonge, J., Mori, W. B., & Silva, L. O. 2012, PhRvL, 108, 235004
Fonseca, R. A., Silva, L. O., Tsung, F. S., et al. 2002, LNCS, 2331, 342
Fonseca, R. A., Vieira, J., Fiuza, F., et al. 2013, PPCF, 55, 124011
Fried, B. D. 1959, PhFl, 2, 337
Garasev, M., & Derishev, E. 2016, MNRAS, 461, 641
Gedalin, M., Smolik, E., Spitkovsky, A., & Balikhin, M. 2012, EL, 97, 35002
Godfrey, B. B. 1974, JCoPh, 15, 504
Godfrey, B. B., & Vay, J.-L. 2013, JCoPh, 248, 33
Hascoët, R., Vurm, I., & Beloborodov, A. M. 2015, ApJ, 813, 63
Haugbølle, T. 2011, ApJL, 739, L42
Honda, M., Meyer-ter-Vehn, J., & Pukhov, A. 2000, PhPl, 7, 1302
Hoshino, M., & Arons, J. 1991, PhFlB, 3, 818
Hoshino, M., Arons, J., Gallant, Y. A., & Langdon, A. B. 1992, ApJ, 390, 454
Kato, T. N. 2005, PhPl, 12, 080705
Keshet, U., Katz, B., Spitkovsky, A., & Waxman, E. 2009, ApJL, 693, L127
Kumar, R., Eichler, D., & Gedalin, M. 2015, ApJ, 806, 165
Lemoine, M. 2015, JPlPh, 81, 455810101
Lemoine, M., Gremillet, L., Pelletier, G., & Vanthieghem, A. 2019a, PhRvL, 123, 035101
Lemoine, M., & Pelletier, G. 2010, MNRAS, 402, 321
Lemoine, M., & Pelletier, G. 2011, MNRAS, 417, 1148
Lemoine, M., Pelletier, G., Gremillet, L., & Plotnikov, I. 2014, MNRAS, 440, 1365
Lemoine, M., Vanthieghem, A., Pelletier, G., & Gremillet, L. 2019b, PhRvE, 100, 033209
Levinson, A. 2020, PhRvE, 102, 063210
Lyubarsky, Y., & Eichler, D. 2006, ApJ, 647, 1250
Martins, S. F., Fonseca, R. A., Silva, L. O., & Mori, W. B. 2009, ApJ, 695, L189
Medvedev, M. V., Fiore, M., Fonseca, R. A., Silva, L. O., & Mori, W. B. 2005, ApJL, 618, L75
Medvedev, M. V., & Loeb, A. 1999, ApJ, 526, 697
Mészáros, P., Ramirez-Ruiz, E., & Rees, M. J. 2001, ApJ, 554, 660
Naseri, N., Bochkarev, S. G., Ruan, P., et al. 2018, PhPl, 25, 012118
Nishikawa, K. I., Niemiec, J., Hardee, P. E., et al. 2009, ApJL, 698, L10
Pelletier, G., Bykov, A., Ellison, D., & Lemoine, M. 2017, SSRv, 207, 319
Pelletier, G., Gremillet, L., Vanthieghem, A., & Lemoine, M. 2019, PhRvE, 100, 013205
Pelletier, G., Lemoine, M., & Marcowith, A. 2009, MNRAS, 393, 587
Peterson, J. R., Glenzer, S., & Fiuza, F. 2021, PhRvL, 126, 215101
Peterson, J. R., Glenzer, S., & Fiuza, F. 2022, ApJL, 924, L12
Plotnikov, I., Grassi, A., & Grech, M. 2018, MNRAS, 477, 5238
Plotnikov, I., Pelletier, G., & Lemoine, M. 2011, A&A, 532, A68
Plotnikov, I., Pelletier, G., & Lemoine, M. 2013, MNRAS, 430, 1280
Ramirez-Ruiz, E., Nishikawa, K.-I., & Hededal, C. B. 2007, ApJ, 671, 1877
Ruyer, C., & Fiuza, F. 2018, PhRvL, 120, 245002
Ruyer, C., Gremillet, L., & Bonnaud, G. 2015a, PhPl, 22, 082107
Ruyer, C., Gremillet, L., Bonnaud, G., & Riconda, C. 2017, PhPl, 24, 041409
Ruyer, C., Gremillet, L., Debayle, A., & Bonnaud, G. 2015b, PhPl, 22, 032102
Shaisultanov, R., Lyubarsky, Y., & Eichler, D. 2012, ApJ, 744, 182
Silva, L. O., Fonseca, R. A., Tonge, J. W., et al. 2003, ApJL, 596, L121
Sironi, L., Spitkovsky, A., & Arons, J. 2013, ApJ, 771, 54
Spitkovsky, A. 2005, in AIP Conf. Ser. 801, Astrophysical Sources of High Energy Particles and Radiation, ed. T. Bulik, B. Rudak, & G. Madejski (Melville, NY: AIP), 345
Spitkovsky, A. 2008a, ApJL, 682, L5
Spitkovsky, A. 2008b, ApJL, 673, L39
Stockem, A., Fiúza, F., Fonseca, R. A., & Silva, L. O. 2012, ApJ, 755, 68
Stockem Novo, A., Bret, A., Fonseca, R. A., & Silva, L. O. 2015, ApJL, 803, L29
Takamoto, M., Matsumoto, Y., & Kato, T. N. 2018, ApJL, 860, L1
Thompson, C., & Madau, P. 2000, ApJ, 538, 105
Vanthieghem, A., Lemoine, M., & Gremillet, L. 2018, PhPl, 25, 072115
Vanthieghem, A., Lemoine, M., Plotnikov, I., et al. 2020, Galax, 8, 33
Vanthieghem, A., Mahlmann, J. F., Levinson, A., et al. 2022, MNRAS, 511, 3034
Weibel, E. S. 1959, PhRvL, 2, 83